The Journal of Undergraduate Research in Physics

The opereations of the Journal are being reviewed by the American Institute of Physics. Please send any comments you have about the Journal and its contents to the chair of the review committee:

Dr. Robert Romer, Chair, JURP Review Committee
Merrill Science Building, Room 222
Amherst College
Amherst, MA 01002

Volume 14, Number 1
December, 1995

Published by the Physics Department of Guilford College
for
The American Institute of Physics and the Society of Physics Students

THE JOURNAL OF UNDERGRADUATE RESEARCH IN PHYSICS

This journal is devoted to research work done by undergraduate students in physics and its related fields. It is to be a vehicle for the exchange of ideas and information by undergraduate students. Information for students wishing to submit manuscripts for possible inclusion in the Journal follows.

ELIGIBILITY
The author(s) must have performed all work reported in the paper as an undergraduate student(s). The subject matter of the paper is open to any area of pure or applied physics or physics related field.

SPONSORSHIP
Each paper must be sponsored by a full-time faculty member of the department in which the research was done. A letter from the sponsor, certifying that the work was done by the author as an undergraduate and that the sponsor is willing to be acknowledged at the end of the paper, must accompany the manuscript if it is to be considered for publication.

SUBMISSION
Two copies of the manuscript, the letter from the sponsor and a telephone number or E-Mail address where the author can be reached should be sent to:

Dr. Rexford E. Adelberger, Editor
THE JOURNAL OF UNDERGRADUATE
RESEARCH IN PHYSICS
Physics Department
Guilford College
Greensboro, NC 27410

FORM
The manuscript should be typed, double spaced, on 8 1/2 x 11 inch sheets. Margins of about 1.5 inches should be left on the top, sides, and bottom of each page. Papers should be limited to fifteen pages of text in addition to an abstract (not to exceed 250 words) and appropriate drawings, pictures, and tables.

Manuscripts may be submitted on a disk that can be read by a MacIntosh™. The files must be compatible with MacWrite™, MicroSoft Word™ , PageMaker™ or WordPerfect™.

ILLUSTRATIONS
Line drawings should be made with black ink on plain white paper. Each figure or table must be on a separate sheet. Photographs must have a high gloss finish. If the submission is on a disk, the illustrations should be in PICT, TIFF or EPS format.

CAPTIONS
A brief caption should be provided for each illustration or table, but it should not be part of the figure. The captions should be listed together at the end of the manuscript

EQUATIONS
Equations should appear on separate lines, and may be written in black ink. We use EXPRESSIONIST™ to format equations in the Journal.

FOOTNOTES
Footnotes should be typed, double spaced and grouped together in sequence at the end of the manuscript.

PREPARING A MANUSCRIPT
A more detailed set of instructions for authors wishing to prepare manuscripts for publication in the Journal of Undergraduate Research in Physics can be found in Volume 8 #1 which appeared in October of 1989 or in Volume 11 #2 which appeared in May of 1993.

SUBSCRIPTION INFORMATION

The Journal is published twice each academic year, issue # 1 appearing in November and issue # 2 in May of the next year. There are two issues per volume.

TYPE OF SUBSCRIBER	PRICE PER VOLUME
Individual	$US 5.00
Institution	$US 10.00

Foreign subscribers add $US 2.00 for surface postage, $US 10.00 for air freight.

Back issues may be purchased by sending $US 15.00 per volume to the editorial office.

To receive a subscription, send your name, address, and check made out to **The Journal of Undergraduate Research in Physics (JURP)** to the editorial office:

JURP
Physics Department
Guilford College
Greensboro, NC 27410

The Journal of Undergraduate Research in Physics is sent to each member of the Society of Physics Students as part of their annual dues.

VOLUME 14
ACADEMIC YEAR 1995-1996

The Journal of Undergraduate Research in Physics

ISSN 0731 - 3764

Published by the Physics Department
of Guilford College
for
The American Institute of Physics
and
The Society of Physics Students

NEUTRON SCATTERING: THE PÖSCHL-TELLER POTENTIAL

Dan Adrian Mazilu * and Andrei Teodor Filip **
Physics Department
University of Nebraska at Omaha
Omaha, NE 68182-0266
received August 12, 1994

ABSTRACT

In the present paper, the Pauli spinor equations are solved for a neutron beam moving in a spatially varying magnetic field whose magnitude is determined by the Pöschl-Teller potential. Transmission and reflection amplitudes were calculated and plotted for both spin states in the case of the finite range potential as well as for the infinite range potential. Spin dependent effects and features manifested in the special characteristics of the potential are discussed.

INTRODUCTION

Spin dependent effects in the transmissivity and reflectivity of a neutron beam passing through a constant magnetic field band were discussed in a previous paper. [1] This paper showed that, contrary to what is expected in a classical mechanical system, different effects occurred for neutrons of opposite spins when the magnetic moments were perpendicular to the external magnetic field. In this paper, using the analytical potential:

$$V(x) = \frac{U_o}{\cosh^2 \alpha x} \qquad (1)$$

where U_o and α are the parameters of the potential, we demonstrate that the same effect persists when the magnetic field strength is a spatially varying function. This potential was first introduced by Pöschl and Teller [2] to study the vibrational spectra of polyatomic molecules. The necessary analytical wave functions for the bound state (E<0) and the continuous state (E>0) were found in the classic quantum mechanics text written by Landau and Lifshitz. [3]

Dan is a senior applied physics major at the University Ioan Cuza, the oldest university in Romania. He just finished his senior project and will graduate by the end of 1995. He plans to pursue his graduate study in the United States in experimental solid state physics. Andrei is a junior applied physics major at the same university. He will work on his project next summer and will graduate by the end of 1996. This research work was performed during their stay at the University of Nebraska at Omaha in the summer semester of 1994. They came to UNO as exchange students and spent eight months in Omaha.

THEORY AND DISCUSSION

We assume a neutron beam emerging from the -x direction, carrying momentum pointing in the +x direction. The spin of the neutron is either pointing in the +y or -y direction (into or out of the page). The neutrons are traveling , as shown in Figure 1, in a spatially varying magnetic field given by:

$$\boldsymbol{B}(x) = \frac{B_o \hat{z}}{\cosh^2 \alpha x} , \qquad (2)$$

where B_o is the strength of the magnetic field, $\hat{z}$ is the unit vector in the z direction and $1/\alpha$ is the effective range of the magnetic field.

The kinetic energy, E, of the neutrons is given by:

$$E = \frac{(\hbar k)^2}{2m} , \qquad (3)$$

where m is the mass of the neutron and k is the size of the wave vector. The potential energy, U, of the interaction between the magnetic moment of the neutron, μ_n, with the magnetic field, $\boldsymbol{B}(x)$, is given by:

$$U = -\mu_n \cdot \boldsymbol{B}(x) \quad \text{where} \quad \mu_n = -1.91 \frac{e h}{2 m c} . \qquad (4)$$

The negative sign in Equation 4 is due to the special characteristics of the neutron: the direction of the magnetic moment was found experimentally to be opposite to that of its spin angular momentum.

As discussed in a previous paper [1], the spin states pointing in the +y and -y directions can be expressed as a linear combination of the spin states pointing in the +z and -z directions. Thus, in contrast to a classical mechanical view, the neutrons whose spins are pointing in the +y and -y directions can have their spin components parallel and antiparallel to the magnetic field direction (the +z direc-

tion). Hence, the interaction with the magnetic field $\boldsymbol{B}(x)$ can be written as:

$$U_{\downarrow\uparrow}(x) = \pm \boldsymbol{\mu}_n \cdot \boldsymbol{B}(x) \tag{5}$$

Therefore, the Hamiltonian operator for the system can be written as:

$$H_{\downarrow\uparrow} = -\frac{\hbar^2}{2m}\frac{d^2}{dx^2} \pm \frac{\mu_n B}{\cosh^2 \alpha x} \tag{6}$$

The entire scattering experiment can be described by letting $\mu_n B = U_o$ and using the results in Landau's text [3].

When the incident energy $E>0$,

$$k = \sqrt{\frac{2mE}{\hbar}} \tag{7}$$

In the case where the spin is antiparallel to direction of the magnetic field, the incident particle 'sees' a potential barrier as shown in Figure 1 (upper curve). If $\frac{8mU_o}{\hbar^2\alpha^2} < 1$, the transmissivity, $\mathcal{T}$, and the reflectivity, $\mathcal{R}$, for the infinite range potential are:

$$\mathcal{T} = \frac{\sinh^2\left(\frac{\pi k}{\alpha}\right)}{\sinh^2\left(\frac{\pi k}{\alpha}\right) + \cos^2\left(\frac{\pi}{2}\sqrt{1-\frac{8mU_o}{\hbar^2\alpha^2}}\right)}$$

$$\mathcal{R} = \frac{\cos^2\left(\frac{\pi}{2}\sqrt{1-\frac{8mU_o}{\hbar^2\alpha^2}}\right)}{\sinh^2\left(\frac{\pi k}{\alpha}\right) + \cos^2\left(\frac{\pi}{2}\sqrt{1-\frac{8mU_o}{\hbar^2\alpha^2}}\right)} \tag{8}$$

If $\frac{8mU_o}{\hbar^2\alpha^2} > 1$, then $\mathcal{T}$ and $\mathcal{R}$ become:

$$\mathcal{T} = \frac{\sinh^2\left(\frac{\pi k}{\alpha}\right)}{\sinh^2\left(\frac{\pi k}{\alpha}\right) + \cosh^2\left(\frac{\pi}{2}\sqrt{\frac{8mU_o}{\hbar^2\alpha^2}-1}\right)}$$

$$\mathcal{R} = \frac{\cosh^2\left(\frac{\pi}{2}\sqrt{\frac{8mU_o}{\hbar^2\alpha^2}-1}\right)}{\sinh^2\left(\frac{\pi k}{\alpha}\right) + \cosh^2\left(\frac{\pi}{2}\sqrt{\frac{8mU_o}{\hbar^2\alpha^2}-1}\right)} \tag{9}$$

When the spin is aligned with the magnetic field, then $E < 0$, so the particle is passing through a potential well instead of a potential barrier, lower curve in figure 1. Then, the transmissivity and the reflectivity become:

$$\mathcal{T} = \frac{\sinh^2\left(\frac{\pi k}{\alpha}\right)}{\sinh^2\left(\frac{\pi k}{\alpha}\right) + \cos^2\left(\frac{\pi}{2}\sqrt{1-\frac{8mU_o}{\hbar^2\alpha^2}}\right)}$$

$$\mathcal{R} = \frac{\cos^2\left(\frac{\pi}{2}\sqrt{1-\frac{8mU_o}{\hbar^2\alpha^2}}\right)}{\sinh^2\left(\frac{\pi k}{\alpha}\right) + \cos^2\left(\frac{\pi}{2}\sqrt{1-\frac{8mU_o}{\hbar^2\alpha^2}}\right)} \tag{10}$$

Here, unlike in Equations 8 and 9, U_o is negative. A bit of algebra shows that:

$$\mathcal{T} + \mathcal{R} = 1\ , \tag{11}$$

flux conservation is guaranteed in both cases.

Most interesting is the case when

$$1 + \frac{8m|U_o|}{\hbar^2\alpha^2} = (2n+1)^2\ ,\ n = 1,2,3... \tag{12}$$

Then

$$\mathcal{T} = 1 \quad \text{or} \quad \mathcal{R} = 0 \tag{13}$$

Thus, for certain values of the depth of the well, the particles passing over it are not reflected and the potential becomes "reflectionless" [4]. In our case, the complete transmission will occur at certain magnitudes of the magnetic field.

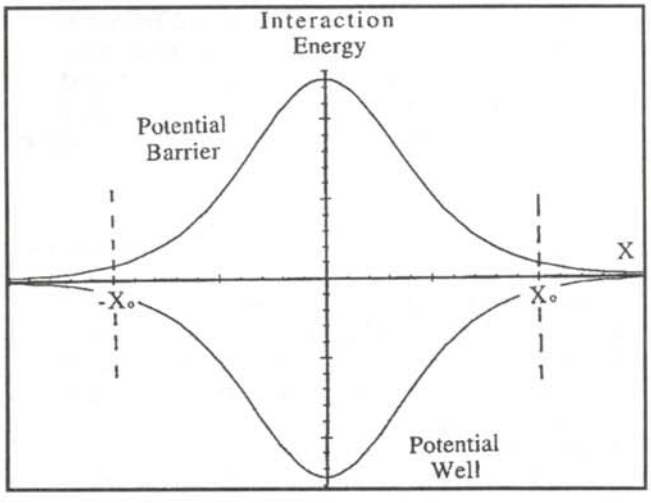

Figure 1
Pöschl-Teller potential described by Equation 1. The finite range potential has the same V(x) when $|x|<x_o$, but equal to 0 when $|x|>x_o$.

The presentation in Landau's text provides us with more information that just the wave functions for the infinite range case. We also can obtain the transmission and reflection coefficients for a finite range Pöschl-Teller potential, which is relevant for our purpose. Consider the finite range potential when the magnetic moment is parallel to the magnetic field:

$$U_{\uparrow}(x) = -\frac{U_o}{\cosh^2 \alpha x} \quad for |x| < x_o$$
$$= 0 \qquad for |x| > x_o \ , \tag{14}$$

where $U_o = \mu B > 0$ and x_o is the range of the potential. The incident wave, which is coming from the left and moving to the right, together with the reflected wave determine the wave function for the region $x < -x_o$:

$$\Psi_1(x) = e^{ikx} + R\, e^{-ikx} \ , \tag{15}$$

where R is the amplitude of the reflected wave. In the region $x > x_o$, the transmitted wave is given by:

$$\Psi_{111}(x) = T\, e^{ikx} \ , \tag{16}$$

where T is the amplitude of the transmitted wave. The total wave function inside the region where $|x| < x_o$ can be written as:

$$\Psi(x) = A\, \Psi_R(x) + B\, \Psi_L(x) \ , \tag{17}$$

where

$$\Psi_R(x) = \left(1-\xi^2\right)^{-\frac{ik}{2\alpha}} \cdot F\left[\left(-\frac{ik}{\alpha} - S\right), \left(-\frac{ik}{\alpha} + S + 1\right); \left(-\frac{ik}{\alpha} + 1\right); \left(\frac{1-\xi}{2}\right)\right]$$
$$\Psi_L(x) = \left(1-\xi^2\right)^{\frac{ik}{2\alpha}} \cdot F\left[\left(\frac{ik}{\alpha} - S\right), \left(\frac{ik}{\alpha} + S + 1\right); \left(\frac{ik}{\alpha} + 1\right); \left(\frac{1+\xi}{2}\right)\right] \tag{19}$$

and

$$ik = \sqrt{-\frac{2mE}{\hbar^2}} \quad \text{and} \quad E > 0$$
$$S = \frac{1}{2}\left(-1 + \sqrt{1 + \frac{8mU_o}{\hbar^2 \alpha^2}}\right) \tag{20}$$
$$\xi = \tanh(\alpha x)$$

$F(a,b;c;z)$ is the hypergeometric function, defined as: [5]

$$F(a,b;c;z) = 1 + \frac{ab}{c} z + \frac{a(a+1)\, b(b+1)}{c(c+1)} \frac{z^2}{2!} + \ldots \tag{21}$$

$\Psi_R(x)$ and $\Psi_L(x)$ were chosen to satisfy the proper asymptotic behavior:

$$\Psi_R(x) \approx e^{ikx} \quad x \to \infty$$
$$\Psi_L(x) \approx e^{-ikx} \quad x \to -\infty \ . \tag{22}$$

When the limits are reversed, we get the expressions shown in Landau's text, implying that:

$$\Psi_R(x) = \Psi_L^*(-x) \tag{23}$$

It can be shown that wave functions of Equation 19 reduce to the infinite range case when $x_o \to \infty$.

To find expressions for T and R, the amplitudes of the transmitted and reflected waves, in the finite range case, we used the continuity conditions of the wave functions and their derivatives at the boundies ($x = \pm x_o$). After tedious manipulations, and making use of recurrence relationships for the hypergeometric function such as:

$$\frac{d}{dz} F(a,b;c;z) = \frac{ac}{c} F(a+1, b+1; c+1; z) \ , \tag{24}$$

the expressions for the transmission and reflection coefficients obtained are:

$$T = e^{-2ikx_o} \frac{\Psi_-^* \Phi_+^* + \Phi_-^* \Psi_+^*}{\Phi_- \Phi_+^* - \Psi_- \Psi_+^*} \frac{W}{W^*} \tag{25}$$

$$R = e^{-2ikx_o} \frac{\Psi_-^* \Psi_- + \Phi_-^* \Phi_-}{\Psi_+^* \Psi_- - \Phi_+^* \Phi_-} \ , \tag{26}$$

where

$$\Psi_+(x) = \frac{d\Psi_R(x)}{dx} + ik\, \Psi_R(x)$$
$$\Psi_-(x) = \frac{d\Psi_R(x)}{dx} - ik\, \Psi_L(x)$$
$$\Phi_+(x) = \frac{d\Psi_L(x)}{dx} + ik\, \Psi_R(x) \tag{27}$$
$$\Phi_-(x) = \frac{d\Psi_L(x)}{dx} - ik\, \Psi_R(x) \ ,$$

and W, is the Wronskian:

$$W(x) = \Psi_R(x) \frac{d\Psi_L(x)}{dx} - \frac{d\Psi_R(x)}{dx} \Psi_L(x) \ . \tag{28}$$

The transmissivity, $\mathcal{T}$, and reflectivity, $\mathcal{R}$, are found from T and R (Equations 25 and 26) by:

$$\mathcal{T} = |T|^2 \qquad \mathcal{R} = |R|^2 \tag{29}$$

It is not obvious that flux conservation still holds in the case we presented, but we verify it numerically later in the paper.

If the magnetic moment is aligned antiparallel to the magnetic field, the neutron 'sees' a different potential:

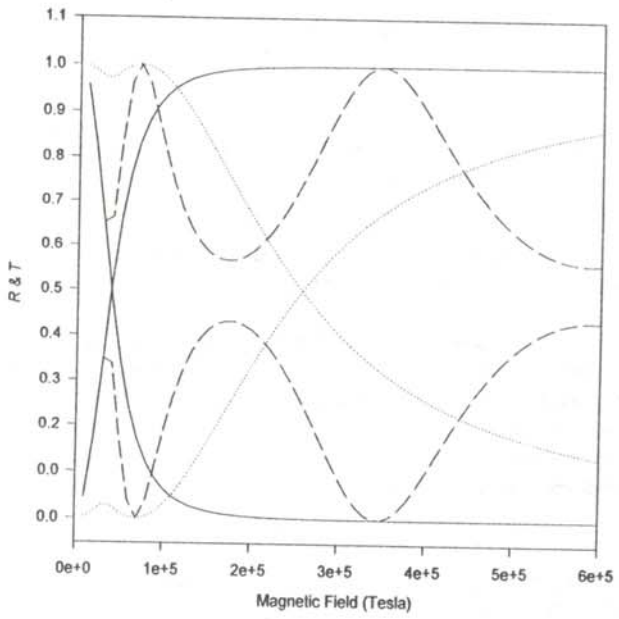

Figure 2

Reflectivity, $\mathcal{R}$, (lower curves) and transmissivity, $\mathcal{T}$, (upper curves) coefficients for the parallel case (or potential well) as a function of the magnetic field (1 - 40 T). The energy of the incoming neutron beam is 2.7x10-7 eV and the characteristic length of the magnetic field is 50 Å. The solid lines are for the infinite range potential while the dashed ones are for a finite range of 200 Å. The oscillatory behavior of the coefficients is evident.

$$U_{\downarrow}(x) = \frac{U_o}{\cosh^2 \alpha x} \quad for\,|x| < x_o$$
$$= 0 \qquad for\,|x| > x_o\ , \tag{30}$$

where $U_o = \mu_n B_o > 0$. The same analysis can be performed for the antiparallel case, except that

$$S = \frac{1}{2}\left(-1 + \sqrt{1 - \frac{8\,m\,U_o}{\hbar^2\,\alpha^2}}\right) \text{ when } \frac{8\,m\,U_o}{\hbar^2\,\alpha^2} < 1 \tag{31}$$

or

$$S = \frac{1}{2}\left(-1 + \sqrt{\frac{8\,m\,U_o}{\hbar^2\,\alpha^2} - 1}\right) \text{ when } \frac{8\,m\,U_o}{\hbar^2\,\alpha^2} > 1. \tag{32}$$

Therefore, the results are the same as those shown in Equations 18-20 with the values of S replaced.

NUMERICAL RESULTS

Computer programs were written to generate data and graphs for the various reflectivity and transmissivity coefficients as a function of the magnetic field for both spin states. In Figure 2, we observe very prominent oscillations in the transmissivity and reflectivity coefficients for the antiparallel case (potential well) for both the finite and infinite range Pöschl-Teller potentials. The magnitudes of these oscillations are proportional to the magnetic field strength. In Figure 3, using the same set of parameters, we show that for the infinite range potential, the transmissivities and reflectivities for the parallel case (potential barrier) vary monotonously with the strength of the magnetic field. Even though it is not obvious, we found that the numerical values of $\mathcal{T}$ and $\mathcal{R}$ in Figures 2 and 3 always added up to unity, a fact that ensures the flux conservation.

The characteristic length of the potential, $1/\alpha$, was chosen to be 50 Å, roughly the size of a flux vortex in a high temperature superconducdtor. To enhance the oscillatory features in the transmissivity and reflectivity coefficients, the kinetic energy of the neutron beam was chosen to be 2.7x10-7 eV, the same order of magnitude as the potential energy of the particle in the magnetic field. A neutron beam with such a low kinetic energy is practically impossible to achieve in an experiment. Even if we reduce the width of the magnetic field distribution to as little as 1 Å and increase the magnetic field up to 3x10⁴ T, about 100 times larger than the highest magnetic field produced in the laboratory, the kinetic energy becomes only 7.5x10-4 eV. In view of this situation, unless we can increase the magnetic field and discover a light neutral particle with a giant magnetic moment, the scattering

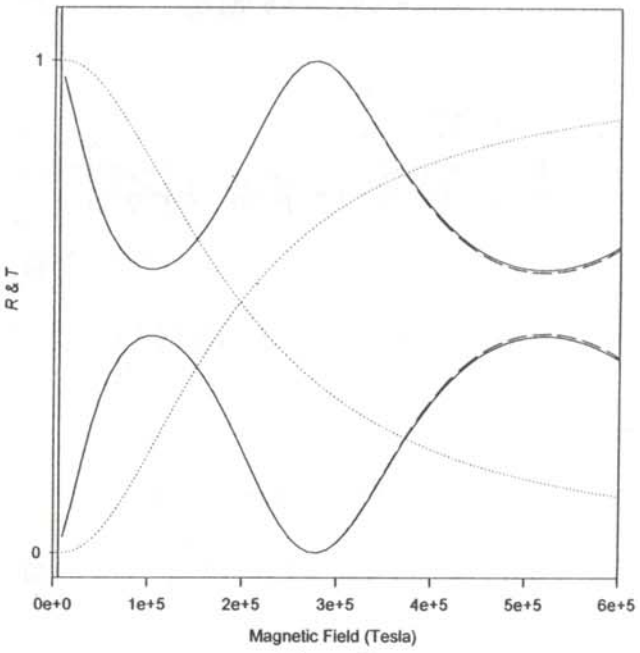

Figure 3

Reflection (lower curves) and transmission (upper curves) for the antiparallel case (or potential barrier) as a function of the magnetic field (1 - 40 T). The energy of the incoming neutron beam is 2.7x10-7 eV and the characteristic length of the magnetic field is 50 Å. The solid lines are for the infinite range potential, while the dashed ones are for the finite range. Notice the difference in behavior between the finite and infinite range potentials.

experiment will remain 'gedanken'.

In Figure 4, we present a three dimensional plot of the spin parallel reflectivity as a function of the kinetic energy and the magnetic field strength. The results show the existence of the reflectionless regions in the case of the finite range Pöschl-Teller potential, regions similar to those described by Equations 12 and 13 for the case of the infinite range potential.

ACKNOWLEDGMENTS

The authors would like to express their appreciation for Dr. Glen Sowell's technical help in using the MAPLE™ software.

REFERENCES

* current address of the author: Dan Mazilu, Soceaua Nationala 51, B1.C2, Sc.B, Apt.12, Iasi 6600, Romania. dmazilu@uaic.ro:

** current address of author: Andrei Filip, Soseaua T. Neculai 7, Iasi 6600, Romania. afilip@uaic.ro

1. T.D. Burnes II and S.L. Stenberg, The Journal of Undergraduate Research in Physics, 12, 1, (1993), pp. 11-14.
2. G. Pöschl and E. Teller, Z. Physik, 83, (1933), p. 143.
3. L.D. Landau and E.M. Lifshitz, Quantum Mechanics, Nonrelativistic Theory, Pergamon Press, (1962).
4. W. van Digk and K.A. Kiers, American Journal of Physics, 60, (1992), p. 520.
5. M Abramowitz and I.A. Stegun, Handbook of Mathematical Functions, Dover Publications, (1972).

FACULTY SPONSOR

Dr. Wai-Ning Mei
Department of Physics
University of Nebraska at Omaha
Omaha, NE 68182-0266
physmei@cwis.unomaha.edu

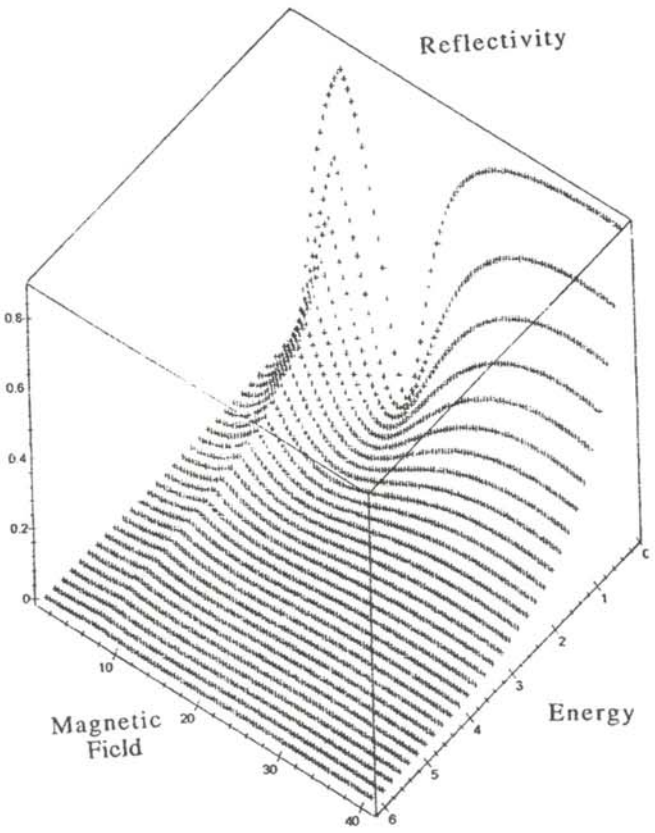

Figure 4
Reflectivity, $\mathcal{R}$, for the parallel case plotted as a function of the energy, E, of the incoming neutron (0 - 6x10^{-4} eV) and the external magnetic field (0 - 40 T). The characteristic length of the potential is 50 Å and the range of the potential is 200 Å.

STATISTICAL ANALYSIS OF THE $^{12}C(^{13}C,\alpha)^{21}Ne$ NUCLEAR REACTION

Michael T. Nimchek and Amy Snyder Hale †
Department of Physics
University of Richmond
Richmond, VA 23173
received August 1, 1994

ABSTRACT

Complete differential cross sections for the $^{12}C(^{13}C,\alpha)^{21}Ne$ reaction were taken at laboratory bombarding energies ranging from 15.250 MeV to 17.875 MeV. To determine if 'nuclear' molecules are formed in these collisions, the data were subjected to statistical tests to filter out true resonances from background reactions. The autocorrelation function, Y_{D_K} analysis, angular cross correlation, probability distribution and the summed deviation function were used. The results of the analysis indicate a significant direct component and a strong possibility of resonance.

INTRODUCTION

Prior to 1960, it was assumed that when heavy nuclei collided, one of two things would happen. The nuclei could collide head on and form a state known as a compound nucleus. This is a thermally equilibrated state where the kinetic energy of the collision is evenly distributed among all the nucleons. Otherwise, the ions would graze each other and the nucleons interact only peripherally, in a manner similar to elastic scattering. A theoretical model , the statistical model, describes the formation of the compound nucleus, while the Born approximation describes the peripheral scattering.

Michael Nimchek is a senior mathematics and physics major at the University of Richmond. He participated in the statistical analysis of these data during the summer following his first year. He is currently applying to graduate school in mathematics and is completing an undergraduate thesis in complex analysis. In his spare time, Michael enjoys studying Any Rand's philosophy of Objectivism.

Amy Snyder received her B.Sc. in physics from the University of Richmond in 1993 and her M.Sc. in physics from the University of Pittsburgh in August of 1995. She is currently working on her Ph.D. in planetary science. Her research is conducted at Pittsburgh's Allegheny Observatory under the direction of George Gatewood. When she has time away from the rigors of graduate school, she shoots her rifle competitively.

For some reactions these models fail because a third possibility arises. The nuclei don't collide head on, yet the collision brings particles close enough for the strong force to overcome the electrostatic repulsion. The nuclei spin in a dumbbell configuration with a large angular momentum before decaying. Such a system is called a nuclear molecule. It was first observed in the collision of low energy ^{12}C nuclei. [1] Since the behavior of nuclear molecules deviates from statistical model predictions, such behavior has been dubbed non-statistical or direct. This paper concentrates on the various statistical tests used to determine if the reaction behaves statistically (according to the statistical model predictions of the thermally equilibrated state) or if it has a direct component that would indicate the formation of nuclear models.

THE EXPERIMENT

A ^{13}C beam and a ^{12}C target were used to determine if, despite the addition of a valence neutron to the ^{12}C core, similar results would be obtained. Our experiment detected decays of ^{25}Mg (the intermediate nucleus formed

	Excitation Energy in ^{21}Ne (MeV)			
ground state	0.0			
excited state	0.351			
excited state	1.746			
multiplet 1	2.789	2.796	2.866	
multiplet 2	3.662	3.734	3.883	
multiplet 3	4.432	4.524	4.684	4.726

Table 1
Excitation energies of states and multiplets in ^{21}Ne.

in the $^{12}C + {}^{13}C$ collision) to $^{21}Ne + \alpha$. Full angular distributions were measured at about 170 angles at 125 keV or 250 keV intervals across a laboratory bombarding energy range of just over 2.5 MeV. Three resolved states and three multiplets in ^{21}Ne were measured. The excitation energies shown in Table 1. The energy resolution of the experiment was not sensitive to the small energy differences between the states in the multiplets.

STATISTICAL ANALYSIS

Direct behavior is difficult to detect because true resonances must be distinguished from statistical fluctuations. One of the signatures of resonant behavior is a large direct component in the cross section that is due to a mechanism different from emission of the α from a thermally equilibrated compound nucleus. Hence, the average behavior can be examined for resonances against a fluctuating background. The autocorrelation function and the probability distribution of cross sections use this method to determine the direct component of the reaction.

Another signature for the formation of nuclear molecules is correlations among different final states in the exit channels. A feature observed in the exit channels would be caused by a resonance in the entrance channel. The summed deviation function measures this behavior. Finally, one expects that if the cross sections are dominated by a direct component, only a few large angular momenta should contribute since the reaction would be peripheral in comparison to what would be expected under thermal equilibrium. The coherence angle obtained from the angular cross correlation is used in this test. [2]

Coherence angle

The coherence angle, $C(\theta,\theta)$ determines the average number of angular momenta contributing to the reaction. According to the statistical model, a wide range of angular momenta should contribute. [3] Thus, a low number would suggest a non-statistical component. To extract the coherence angle, one must first determine the angular cross correlation function for a particular final state. The cross correlation function is defined as:

$$C(\theta,\theta) = \frac{\langle \sigma(E,\theta)\,\sigma(E,\theta')\rangle}{\langle \sigma(E,\theta)\rangle\langle \sigma(E,\theta')\rangle} - 1 \ , \qquad (1)$$

where $\sigma(E,\theta)$ is the differential cross section at energy E and angle θ. [4] The bracket notation denotes the standard average. The differential cross section is proportional to the probability of detecting an event. The coherence angle, θ_C, is equal to half of the maximum value of the angular cross correlation function and is inversely proportional to the number of contributing angular momenta, Δl:[5]

$$\Delta l = \frac{1.4}{\theta_C} \ . \qquad (2)$$

Autocorrelation function

The auto correlation function determines the coherence width that is used in subsequent analysis. It is defined by:

$$R(\Gamma,\varepsilon) = \frac{\langle \sigma(E)\,\sigma(E+\varepsilon)\rangle}{\langle \sigma(E)\rangle\langle \sigma(E+\varepsilon)\rangle} - 1 \ , \qquad (3)$$

where $\sigma(E)$ is the total cross section at a bombarding energy E for a given final state (the result of integrating the measured differential cross sections over all angles), ε is the energy interval and Γ is the coherence width of levels in the compound nucleus. [2] The autocorrelation function can also be calculated by:

$$R(\Gamma,\varepsilon) = \frac{\Gamma^2}{\Gamma^2+\varepsilon^2}\,\frac{1-Y_{D_K}}{N_K} \ , \qquad (4)$$

where N_K is the number of open channels contributing to the reaction and Y_{D_K} is the portion of the cross section due to non-statistical mechanisms in this energy range. [2] The number of open channels has a minimum possible value of unity (at 0°) and at 90° attains its maximum value:

$$N_K(\max) = \begin{cases} \frac{g}{2} & (g \text{ even}) \\ \frac{g+1}{2} & (g \text{ odd}) \end{cases} \qquad (5)$$

$$g = (2i+1)(2I+1)(2i'+1)(2I'+1) \ ,$$

where i is the spin of the target, I is the spin of the projectile, i' and I' are the spins of the α and ^{21}Ne fragments. [6] The direct component of the cross section, Y_{D_K}, can be determined by letting $\varepsilon = 0$ in Equation 4: [4]

$$Y_{D_K} = \left[1 - N_K\,R(\Gamma,0)\right]^{\frac{1}{2}} \ . \qquad (6)$$

The uncertainty in Y_{D_K} is calculated using the uncertainty in the mean square deviation of the autocorrelation function with $\varepsilon = 0$:

$$\Delta R(\Gamma,0) = \sqrt{\frac{1+R(\Gamma,0)}{n}} \ , \qquad (7)$$

where n is the number of data points in the sample. [2] The uncertainty Y_{D_K} is:

$$\frac{\Delta Y_{D_K}}{Y_{D_K}} = \frac{\Delta R(\Gamma,0)}{2\left[1-R(\Gamma,0)\right]} \ . \qquad (8)$$

	Y_{D_K} Analysis				C(θ,θ) Analysis
state		N_K value		$\frac{\Delta Y_{D_K}}{Y_{D_K}}$	Δl
(MeV)	max	mean	min		
0.0	.90	.94	.98.	.13	5.0
0.351	.89	.94	.98	.13	5.0
1.746	.73	.86	.97	.14	6.7
2.789 - 2.866	.95	.97	.99	.13	4.5
3.662 - 3.883	.92	.95	.99	.13	5.5
4.432 - 4.726	.89	.94	.98	.13	6.7

Table 2

Non-statistical component and contributing angular momenta for the $^{12}C(^{13}C,\alpha)^{21}Ne$ reaction

The Y_{D_K} analysis gives a range of percentages that depends upon the number of open channels involved. The minimum number of open channels corresponds to the highest possible direct component, while the maximum number of open channels corresponds to the lowest possible direct component.

Probability distribution function

The probability distribution function is a method of comparing the distribution of the angle integrated cross sections and the results of the Y_{D_K} analysis with statistical model predictions. One plots a histogram of the cross sections against the normalized probability curves determined by the values of Y_{D_K} . The quantity Y_K (not to be confused with Y_{D_K}) is determined for each energy by integrating the differential cross sections to yield a total cross section $\sigma_K(E)$ for a given final state. [2] The value of Y_K is given by:

$$Y_K = \frac{\sigma_K(E)}{\langle \sigma_K(E) \rangle} , \tag{9}$$

where K refers to the different final states and multiplets in ^{21}Ne. The equation for the normalized probability distribution curve is:

$$p(Y_K) = \frac{\frac{N_K}{1-Y_{D_K}}\left[\frac{N_K Y_K}{1-Y_{D_K}}\right]^{N_K-1}}{\left[\frac{N_K\left(Y_K Y_{D_K}\right)^{\frac{1}{2}}}{1-Y_{D_K}}\right]^{N_k-1}} \times$$

$$\exp\left\{-N_K \frac{Y_K + Y_{D_K}}{1-Y_{D_K}}\right\} I_{N_K-1}\left\{\frac{2N_K\left(Y_K Y_{D_K}\right)^{\frac{1}{2}}}{1-Y_{D_K}}\right\} , \tag{10}$$

where N_K is the number of open channels, and I_{N_K-1} is a hyperbolic Bessel function of the first kind with order N_K-1. [3,7]

Summed deviation function

The final statistical test used in this paper is the summed deviation function. It is used to find energy regions that deviate substantially from the average cross sections. Such areas indicate the possibility of correlated behavior. Correlations that are measured in the exit channels would be caused by a resonance mechanism in the entrance channel. The deviation function is:

$$D(E) = \frac{1}{N}\sum_{i=1}^{N}\left[\frac{\sigma_K(E)}{\langle \sigma_K(E) \rangle} - 1\right] , \tag{11}$$

where N is the number of excitation functions (six for us: three resolved states and three unresolved multiplets). [2] Note that the deviation function represents an excursion about the average cross section. To determine what constitutes a "substantial" enough deviation from the average to be considered significantly correlated, the probability density function for the deviation, D, was calculated using the relationship:

$$p(D) = \frac{1}{2\pi}\int_{-\infty}^{+\infty}\left[\prod_{k=1}^{N}\xi^{-N_K}\right]\exp\left[jt\frac{1}{N}\sum_{k=1}^{N}\left(\frac{Y_{DK}}{\xi}\right)+D(E)-1\right]dt$$

$$\xi = 1 - jt\frac{1-Y_{DK}}{NN_K} , \tag{12}$$

where j is the square root of -1. The probability density function, $p(D)$, provides a quantitative measure of the likelihood of a given measured deviation, D. Confidence levels, $Q(\chi_T)$ and $Q(\chi_B)$, must be extracted for this purpose corresponding to the percentage of data points that should be greater than χ_T or less than χ_B according to the relations: [8]

$$Q(\chi_T) = \int_{\chi_T}^{\infty} p(D)\, dD$$

$$Q(\chi_B) = \int_{-\infty}^{\chi_B} p(D)\, dD . \tag{13}$$

RESULTS

Table 2 lists the results of the angular cross correlation function analysis for each final state. There are 4 to 7 angular momentum values, Δl, contributing to the different final states. A reaction behaving according to the statistical model predictions should have 10 or more contributing angular momentum values. [9] These lower numbers deviate from the predictions of the statistical model and

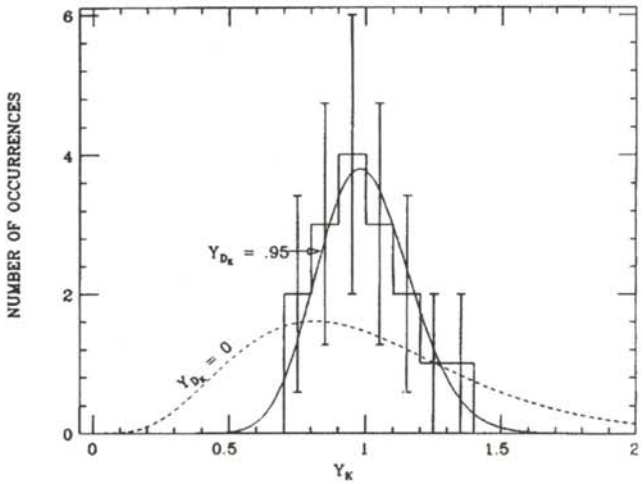

Figure 1

Histogram plot of the distribuiton of cross sections (Y_K) for the second multiplet state. Probability curves are plotted for comparison. The solid curve corresponds to Y_{D_K} = 0.95 while the dashed curve corresponds to Y_{D_K} = 0. The error bars represent the statistical uncertainty in the histogram due to the small number of data points.

suggest the presence of a direct mechanism.

Also listed in Table 2 are the results of the Y_{D_K} analysis for the six energy states and multiplets. Three different values of N_K are calculated corresponding to the minimum N_K=1, the maximum N_K and the average of these values. Notice that the lowest Y_{D_K} value occurs in the second excited state and is still greater than 70%. No other value drops below 85% and most are above 90%. This result implies that most of the cross section is not from the decay of a thermally equilibrated compound nucleus. There is a significant direct component in all the exit channels. Taking the lowest value of Y_{D_K} in each state and subtracting their respective uncertainties still yields values ranging from .59 to .82 Even this 'worst case scenario' still corresponds to a large direct component. These results do not prove the existence of nuclear molecules, but they do mean that a mechanism different from the formation of a thermally equilibrated compound nucleus is at work.

Figure 1 is a histogram of the frequency of the Y_K values for the second multiplet. The results for this state are representative of all six final states and multiplets. The curves in Figure 1 were created by letting Y_{D_K} be a dummy variable in Equation 10. Two Y_{D_K} values were used to create the two different curves. The solid curve represents the calculated Y_{D_K} value that corresponds to the mean value of N_K. The dashed curve represents a statistical model curve, calculated by letting Y_{D_K} go to zero. The solid curve, which represents a Y_{D_K} of 0.95 fits the histogram much better than the dashed curve which represents a purely statistical mechanism. This further supports the existence of direct behavior. There is, however, an inherent ambiguity in the analysis because of the limited number of data points. Each point has an uncertainty of $n^{1/2}$ where n is the number of Y_K counts corresponding to that individual point. The bins only have counts between 1 and 4; these low numbers reflect high uncertainties, but the results are consistent with the results of the other tests.

Figure 2 is a graph of the deviation function versus energy with 3% and 1% confidence levels calculated from the probability density function given by Equation 12. There are 16 points, corresponding to the sixteen different energies. Three percent of these points, or about half a point, should lie above or below the lines if the reaction is a statistical one. We observe three points in this range. Even more important is that two points also lie outside of the 1% confidence level, where the expectation determined by the statistical model is essentially zero. This tests points to the existence of correlated structure in the $^{12}C(^{13}C,\alpha)^{21}Ne$ reaction.

The results of our statistical analysis point to the probable existence of nuclear molecules in the $^{12}C + ^{13}C$ system. The results indicated a significant direct component to the $^{12}C(^{13}C,\alpha)^{21}Ne$ reaction. The Y_{D_K} analysis quantified this direct component as always greater than 70% and usually greater than 90% with an uncertainty of 13%. The results from the probability distribution function favor the non-statistical curves. The deviation function indicates strong correlations that deviate sharply from the behavior of a thermally equilibrated compound nucleus. The angular cross correlation function indicates that a smaller number of angular momentum values are present in the reaction than would be expected according to statistical model predictions. Based on these statistical results, we conclude that the $^{12}C(^{13}C,\alpha)^{21}Ne$ reaction exhibits a substantial direct component that is correlated in many final states. These results are consistent with the formation of nuclear molecules.

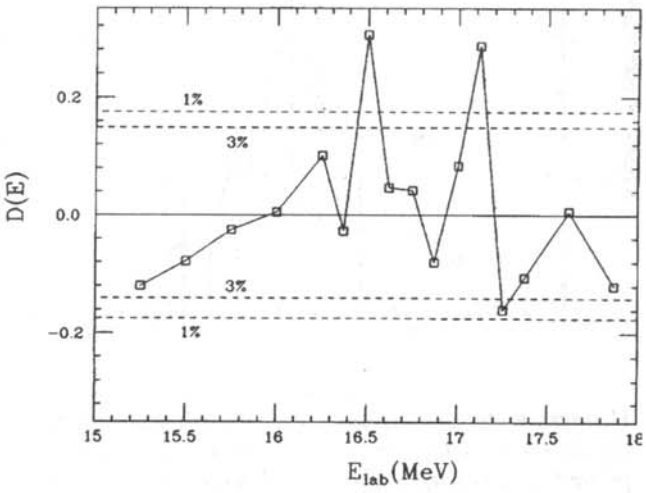

Figure 2
Plot of the summed deviation function versus center-of-mass energy. Confidence levels of 3% and 1% were calculated using the probability density function.

REFERENCES

† present address of author: Amy Snyder Hale, Department of Geology and Planetary Science, University of Pittsburgh, Pittsburgh, PA 15260. assst5+@pitt.edu

1. E. Almqvist, D.A. Bromley, J.A. Kuehner, Phys. Rev. Lett., 4, (1960), p. 515.
2. G.P. Gilfoyle and H.T. Fortune, Phys. Rev., C 32, (1985), p. 865.
3. K.A. Eberhard, Proceedings of the International Conference on the Resonant Behavior of Heavy-Ion Systems, Aegean Sea, 1980, G. Vourvolpoulos, ed, Greek Atomic energy Commission, Athens, (1981) p. 353.
4. G.P. Gilfoyle, Ph.D. thesis, unpublished.
5. P. Braun-Munzinger and J. Barette, Nucl. Phys., 32, (1962), p. 353.
6. T. Ericson, Phys. Rev. Lett., 5, (1963), p. 430.
7. D.M. Brink and R.O. Stephan, Phys. Rev. Lett., 5, (1963), p. 77.
8. J. Lang, M. Hugi, R. Müller, J. Sromicki, E. Ungricht,

H. Witala, L. Jarczyk and A. Stralkowski, Phys. Lett. 104B, (1981), p. 369.
6. A.S. Snyder, G.P. Gilfoyle, C.A. Cardounel, S. Sigworth, C. Smith, R. Zurmühle, H.T. Fortune, J. Arrison, M McKenzie and M. Simpson, Abstract Book: Sixth National Conference on Undergraduate Research, March 26-28,1992, University of North Carolina at Asheville, Asheville. (1993), p. 708.

FACULTY SPONSOR

Dr. Gerard P. Gilfoyle
Department of Physics
University of Richmond
Richmond, VA 23173
GILFOYLE@urvax.urich.edu

THE DIRECTIVITY PATTERN OF A PLANE CIRCULAR DIELECTRIC TRANSDUCER

David W. Coppit
Department of Physics and Astronomy
The University of Mississippi
University, MS 38677
received August 15, 1994

Abstract

Two methods of measuring the directivity pattern of an acoustic transducer are presented, along with experimental data. The first method involves measuring the root mean square voltage from the microphone using a digital oscilloscope and then converting the resulting averaged value to decibels. The second method uses a dynamic signal analyzer to sweep the specified frequencies for a more detailed analysis. The directivity patterns produced are then compared to that of a theoretical infinitely baffled circular piston.

INTRODUCTION

From acoustical theory we know that at low frequencies, speakers act like point sources, radiating sound in all directions equally. But as the frequency increases, the pattern of the intensity of sound in front of the transducer becomes beamed, even exhibiting side lobes. Figure 1 shows a graph, called the directivity pattern, of this intensity as a function of angle from directly in front of the transducer. The graph is assumed to be radially symmetric on the axis of the speaker.

The frequencies at which these effects can be seen are different for speakers of various diameters, so to provide a common basis for comparison between each speaker we must introduce the scaling parameter of *ka*:

$$ka = \frac{2\pi}{\lambda} a = \frac{2\pi f}{c} a \,, \qquad (1)$$

where a is the radius of the transducer, l is the wavelength, f is the frequency, and c is the speed of sound in air. The "Mother of All Speakers" at the University of Mississippi (diameter 2 m) has same directivity pattern as a hearing aid (diameter of 3 mm) at the same values of *ka*, provided the structures of the two transducers are roughly the same.

David Coppit graduated in May of 1995 from the University of Mississippi with Bachelor of Science degrees in both Physics and Computer Science. When he has it, he likes to spend his free time playing the guitar or shooting baskets. One day, he would like to walk the moon in the comfort of his living room.

In our tests, we used a circular dielectric transducer which consists of two plates acting like a capacitor[1]. The plates were made of aluminized mylar stretched across the surface and grounded to the outer casing with silver paint. One of the plates was held immobile. When an alternating voltage was applied across the two plates, the other moved and creates sound waves. The mylar, a dielectric material, is compressed into infinitesimal air pockets on the surface of the back plate when the transducer is operated. Figure 2 is an illustration of a cross-section of the transducer.

The sound levels were measured using a Bruel & Kjaer condenser type microphone, structurally similar to our speaker[2]. A thin membrane, comprising one plate of a capacitor (a back plate is the other), moves with the incoming sound pressure and creates a change in capacitance. Even though the condenser microphone is not exceptionally sensitive, it is popular because of its flat

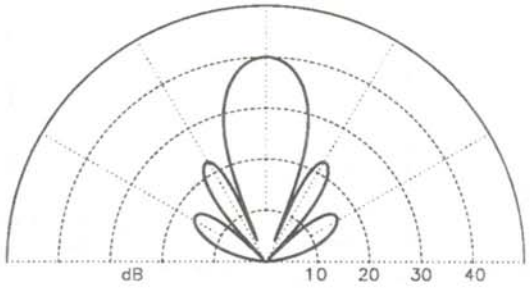

Figure 1
Polar plot of the intensity of an infinitely baffled circular piston with a ka value of 10.

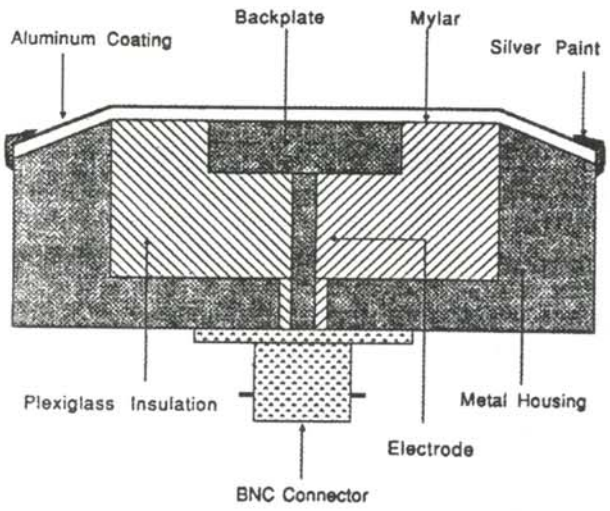

Figure 2
Cross-section of the mylar transducer

frequency response and low self-noise.

THEORY

To polarize the transducer for proper operation, a bias voltage V_o is applied across the "plates". A large resistor is placed between the back plate and the vibrating membrane. This causes the charge on the plates to be unable to change fast enough to respond to the rapidly varying alternating voltage placed across the plates. If we assume the average charge, Q_o, on the plates:

$$Q_o = C_o V_o \ , \qquad (2)$$

then the alternating voltage, V, required to vary the capacitance and cause a resulting movement in the membrane is:

$$V = V_o - \frac{V_o C_o}{C} \qquad (3)$$

where C is the capacitance of the system. A more rigorous examination of the problem can be found in many texts[3].

The directivity of a plane circular piston in an infinitely large rigid wall (a baffle) is produced by diffraction effects. The optical analog is a plane light wave passing through a circular aperture[4]. The resulting sound pressure at a given field point in front of the speaker can be calculated by considering the surface of the speaker to be composed of many small elements, each oscillating with the same phase. The contribution of the pressures from each of the elements are summed in magnitude and phase[5]. The resultant pressure as a function of distance and angle, q, from the axis of the piston is the directivity equation:

$$I = \frac{2 J_1 (ka \sin\theta)}{ka \sin\theta} \ , \qquad (4)$$

where J_1 is the cylindrical Bessel function of order 1.

EXPERIMENTAL SETUP

The measurements were made in an anechoic chamber to avoid extraneous noise and to minimize reflected sound. The transducer was placed in the center of a wheel that could be rotated to allow for measurement of the intensity level at various angles. The microphone was placed in front of the speaker and aimed using its reflection in the aluminum surface. This set up is schematically shown in Figure 3. For the particular speaker we used, an alternating voltage with amplitude of 100 Volts, along with a 200 Volt DC bias, was applied to create the sound.

The first method of measurement consisted of sending a five cycle pulse at a particular frequency to the speaker. The voltage produced by the microphone by the middle three cycles were averaged for about thirty seconds before the rms voltage was measured with the digital oscilloscope. The frequency of the pulse was then manually adjusted to produce several different *ka* values. The wheel was rotated and the procedure repeated.

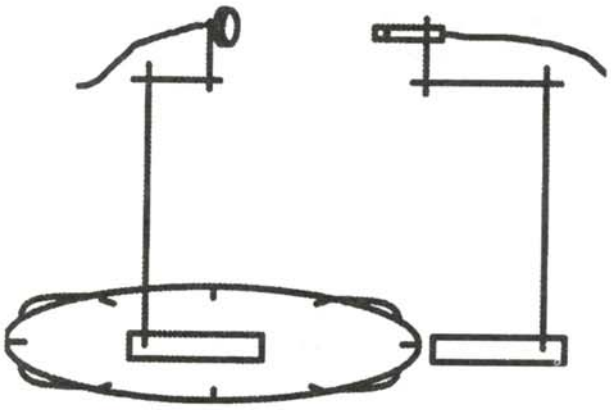

Figure 3
Set up for measuring directivity. The transducer, detailed in figure 2, is in the center, the microphone on the right.

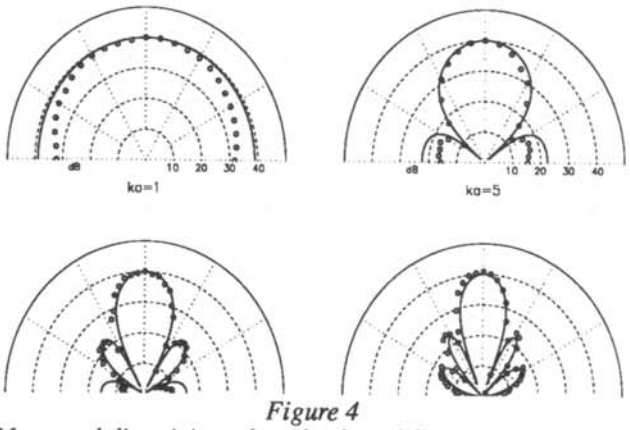

Figure 4
Measured directivity values for four different values of ka. The solid lines are theoretical predictions from Equation 4.

Because the same microphone was used in all the measurements, its frequency response and that of the source were divided out when the voltage values were normalized. This meant that the voltage is a direct indicator of the sound pressure level (SPL):

$$SPL = 20 \log\left(\frac{V}{V_{ref}}\right). \quad (5)$$

The second method again used the same wheel arrangement for the speaker. Instead of pulses, the signal driving the speaker was a continuous tone ramped through a range of frequencies created by a signal generator operating in its swept sine mode. This eliminated the manual adjustment of the frequency, thus speeding up the data taking process.

RESULTS

Figure 4 shows results for values of ka =1, 5, 8, and 10. Also shown are the theoretically calculated directivities for an infinitely baffled circular piston. This model seems to fit the data, except near 90°. At this angle, (except for the ka = 10 data which doesn't exhibit this since its values go to zero at 90°) there seems to be less signal . All values were normalized to 40 dB at zero degrees.

The sweeping method provided many more measurement points that the first method of data collection. In this case, we were able to create a three dimensional graph of the intensity. Figure 5 shows such a plot. The major peak corresponds to the point directly in front of the speaker. For a given frequency, the maxima and minima for the corresponding ka can be observed. For this transducer, a change of 2951 Hz corresponds to a change of ka =1. This means that the graph ranges from $ka \approx 1$ to a value of $ka \approx 13.6$. The noise seen in Figure 5 is caused by the lack of averaging in this method, the trade-off was to get more

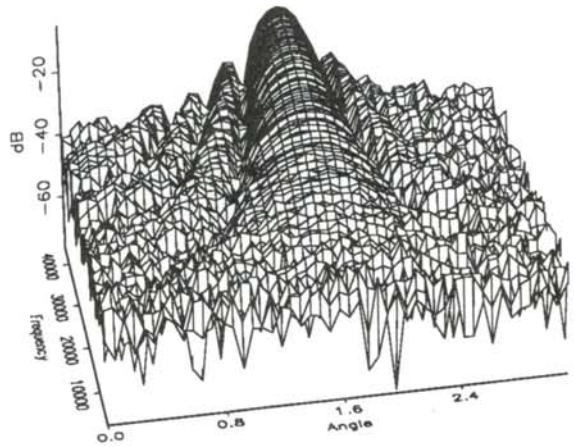

Figure 5
Intensity vs frequency and angle. These are the results from the second method of data collection.

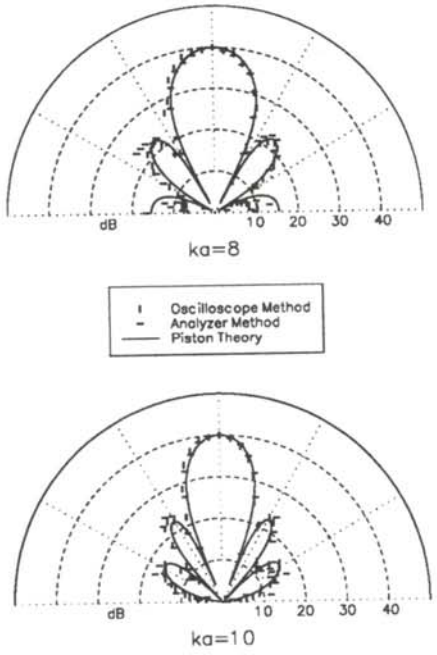

Figure 6
Comparison of the two methods of data collection for two different values of ka.

data points for less sampling time. Note the migration of the nodes toward the center as the frequency increases.

Figure 6 is a comparison of the two techniques for ka = 8 and ka = 10. The method using the sweeping frequency does not seem to display the pronounced decrease in intensity at the sides that the oscilloscope method does. However, both methods exhibit a signal drop at the sides of the speaker, 90° off axis. This implies that in this region, the dielectric transducer's behavior departs from that of the theoretical infinitely baffled piston.

The sweep method data does not seem to follow the ideal calculations as well as the averaged data. Conceivably, the same kind of accuracy as in the oscilloscope experiment could be achieved, but 30 seconds per frequency for 10 frequencies per sweep and a 3.75 degree interval translates to a measuring time of over four hours.

ACKNOWLEDGMENTS

The author appreciated Dr. James Sabatier's guidance and supervision during this project. He also acknowledges the critique of the paper by Dr. Lee Bolen.

REFERENCES

1. Wente, E. C., "A Condenser Transmitter as a Uniformly Sensitive Instrument for the Absolute Measurement of Sound Intensity", Physical Review, 10, (1917), pp. 39-63.

2. Beranek, Leo L., Acoustical Measurements, Leo L. Beranek, (1988), p. 208.
3. Morse, P.M., Vibration and Sound, 2nd ed., McGraw-Hill Book Company, Inc., (1948), pp. 203-213.
4. Hecht, Eugene, Optics, 2nd ed., Addison-Wesley Publishing Company, (1987), pp. 416-421.
5. Morse, P. M., Vibration and Sound, 2nd ed., McGraw-Hill Book Company, Inc., (1948), pp. 326-346.

FACULTY SPONSOR

Dr. James Sabatier
The National Center for Physical Acoustics
The University of Mississippi
University, MS 38655
sabatier@sparc.ncpa.olemiss.edu

ACOUSTIC BRAGG SCATTERING FROM AN ARRAY OF CYLINDRICAL RODS SUSPENDED IN AIR

David W. Coppit*
Department of Physics and Astronomy
The University of Mississippi
University, MS 38677
received August 15, 1994

Abstract

Traditionally, Bragg scattering has been used to study crystals with x-rays where the wavelength and the intermolecular distances are measured in Angstroms. It is our goal to scale up this phenomenon into the centimeter range through the use of ultrasonic acoustic waves and an array of steel bars. In this case, the scattering is two-dimensional instead of the three-dimensional case of atoms in a crystal. We experimentally show that Bragg's Law of scattering also holds for reflection of acoustic waves.

INTRODUCTION

Bragg scattering results when a uniform wave front strikes an evenly spaced array of scatterers[1]. According to Huygen's principle, each member of the array emits wavelets, which add up constructively to form outgoing waves. Figure 1 illustrates this concept, where the scattering centers struck first by the wave radiate first. The larger circles are wavelets that have had time to propagate. The distance between wavelets shown in Figure 1 is one wavelength. The ray diagram, part of Figure 1, shows the resulting paths of the waves.

The intensity of the reflected wave exhibits constructive interference when:

$$2d \sin(\theta) = n \lambda \qquad (1)$$

This is known as Bragg's Law[2], where d is the spacing between scattering centers, θ is the angle from the surface of the array for both the incoming and outgoing waves, n is a positive integer, and λ is the wavelength of the incident wave. As the wave penetrates the array, subsequent rows of scattering centers also radiate causing more than one maximum. For optimum Bragg scattering effects, the spacing d between the scatterers should be on the same order of magnitude as the wavelength of the source of waves.

David Coppit graduated from the University of Mississipi with bachelor of Science degrees in both physics and computer science. When he has it, he likes to spend his free time playing the guitar or shooting baskets. One day, he would like to walk the moon in the comfort of his living room.

Bragg scattering of X-rays, with wavelengths in the Angstrom range, from crystals is typically used to get information about the crystal structure. Another place where Bragg scattering can be observed is in ultrasonic waves in liquids. A transducer is placed on one side of a crystal or a liquid. The ultrasonic waves created by the transducer will generate pressure gradients in the medium that scatter the incident light. This type of diffraction is useful for imaging small objects placed in the ultrasonic beam. The entire image can be seen in the resulting orders of the diffracted beam.

EXPERIMENTAL SETUP

The experimental set up is shown in Figure 2. Our scattering centers were a 10 X 10 array of 1/4 inch bars, suspended at 1 inch intervals between two metal plates. They were hung in an anechoic chamber to isolate the experiment from extraneous noise.

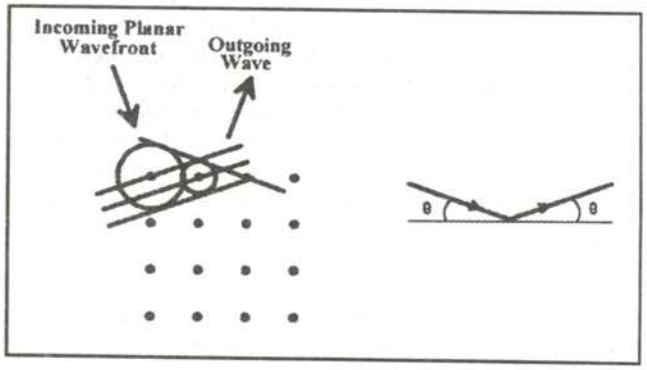

Figure 1
Bragg scattering from a two-dimensional array, showing the wavelets on the left and the ray diagram on the right.

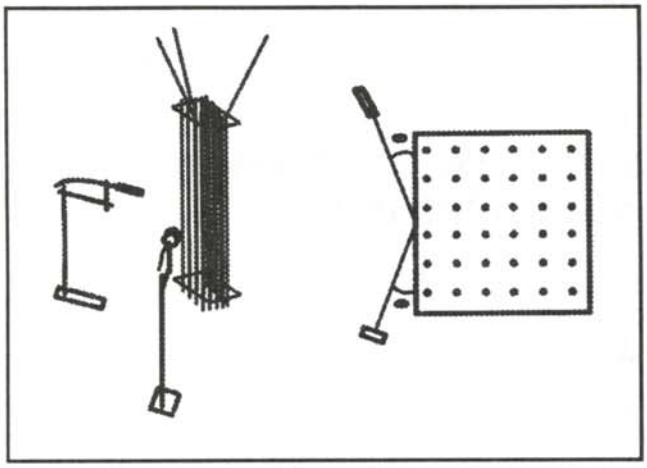

Figure 2
Experimental setup. The diagram on the right is a top view of the setup showing the angle θ

The incident waves were generated using a dielectric capacitor transducer[3]. At a frequency of 29.5 kHz (ka = 10), and 30 inches away, this speaker generates a wave front that is uniform in intensity to within 3 dB over a ten inch span. Since the array is ten inches wide, this transducer effectively generates a plane wave. The speaker was aimed so that it pointed at the center of the first row of scatterers. A Bruel and Kjaer 1/4 inch microphone was aimed at the same location.

To produce the maximum Bragg scattering conditions, we drove the speakers at 13.5 kHz. At this frequency, the wavelength of the incident sound wave is approximately equal to the spacing between the scattering centers.

During the experiment, the intensity at various angles of scattering was examined by moving the microphone and speaker and recording the rms voltage produced by the microphone. This value was converted to dB (using a reference voltage of 1 volt) with

$$SPL = 20 \log\left(\frac{V}{V_{ref}}\right). \qquad (1)$$

The speaker was set up to send tone bursts of five cycles at the specified frequency. Pulses were used so that the direct wave coming from the source would not interfere with the reflection from the array. Some angles (θ less than about 30 degrees) at low frequencies could not be resolved because the distance from the speaker to microphone was almost the same as the distance from the speaker to the array to the microphone; the direct and the reflected waves were interfering.

The voltage produced by the microphone due to the reflected wave was averaged for 30 seconds. The first "start-up" cycle was discarded and the rms voltage was measured over the length of the remaining wave.

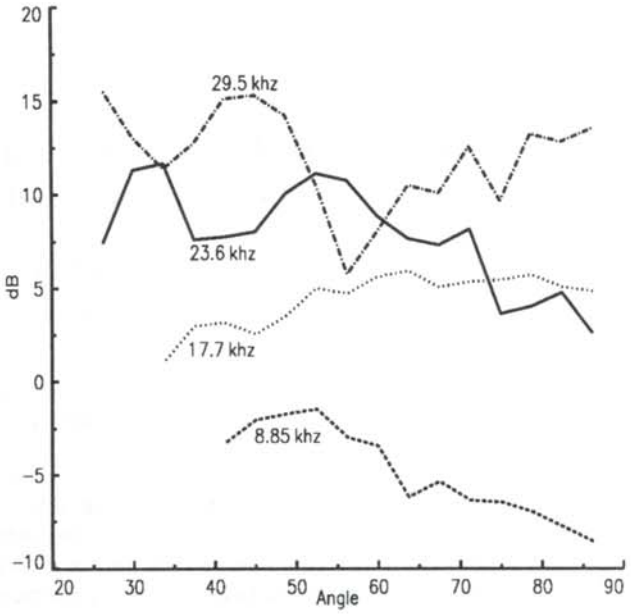

Figure 3
Relative intensity as a function of scattering angle for different frequencies. The Bragg peaks are not evident at low requencies.

RESULTS

Two separate trials were made. The first one investigated the response at four different frequencies. The two frequencies that yielded good results were then investigated in more angular detail. Figure 3 shows the results of the first run. The Bragg scattering model seemed to describe higher frequency results the best. These data meet the condition that the wavelength be comparable to the spacing between scatterers. The lower frequencies had wavelengths that were too long to create the Bragg scattering peaks.

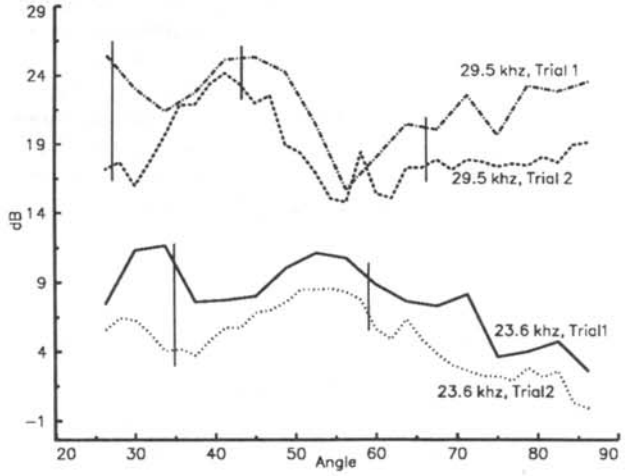

Figure 4
Relative intensity as a function of angle. The top set has a coarser angular resolution than the bottom set.

Figure 4 shows the comparison between the results of the more detailed second trial and the first. The vertical marks are the angular location of the theoretical maxima computed from Equation 1. 10 dB was added to the 29.5 kHz data to make the graph more readable. (The angular coincidence of the maxima is the important factor, not the intensity values). We get at least one good correlation at the expected angle for the 29.5 kHz frequency. The leftmost theoretical peak for the 29.5 kHz graphs occurs near the angle where the interaction between the direct and the reflected waves occurs. The large angle intervals between data points in Trial 1 make it possible that what appears as an upward trend toward a maximum is actually a bad value.

There are two peaks in the 23.6 kHz data that correlate with the expected Bragg peaks. However, the data exhibit maxima about 5 degrees less than expected. One explanation could be that the edges of the supporting plates are reflecting sound that interferes with the signal from the array. This effect may be greater at this frequency than at 29.5 kHz, resulting in a shift in this data alone.

The abnormal results in all the data for angles above 65 degrees may be a consequence of interference of the reflected wave. At these angles, the speaker and microphone are close together. The returning signal from the array may be striking the source, causing subsequent reflected waves.

SUMMARY

The Bragg scattering phenomena is not restricted to atomic sizes. With the use of sound waves and steel bars, it is possible to create the effect macroscopically.

This experiment focused on detecting the reflected waves. But this is not the only type of Bragg scattering. The waves penetrating to subsequent levels of scatterers also create maxima and minima on the far side of the array. Preliminary experiments have not produced positive results. Part of the problem is that there is some ambiguity as to the location of the vertex with which to measure the angles of the maxima.

ACKNOWLEDGMENTS

Thanks are given to Dr. James Sabatier for his support and guidance, as well as to Dr. Mack Breazeale for his insights and criticisms.

REFERENCES

1. Bragg, W. L., *Proceedings of the Royal Society of London*, A88, (1913), p. 428.
2. Elton, L. R. B. and Daphne F. Jackson, "X-Ray Diffraction and the Bragg Law", *American Journal of Physics*, 34, (1966), pp. 1036-1038.
3. Wente, E. C., "A Condenser Transmitter as a Uniformly Sensitive Instrument for the Absolute Measurement of Sound Intensity", Physical Review, 10, (1917), pp. 39-63.

FACULTY SPONSOR

Dr. James Sabatier
The National Center for Physical Acoustics
The University of Mississippi
University, MS 38655
sabatier@sparc.ncpa.olemiss.edu

MORPHOLOGY AND GROWTH OF KIDNEY STONES STUDIED BY LVSEM AND AFM

Hamilton H. Dorian *
Department of Physics and Astronomy
Arizona State University
Tempe, AZ 85287-1504
received September 20, 1994

ABSTRACT

Low voltage scanning electron microscopy and atomic force microscopy were employed for the microscopic examination of two human kidney stones to determine the mechanism of nucleation and growth. High magnification of the stone's surfaces suggested that the stones were not a single crystal but an aggregation of many small crystals.

INTRODUCTION

Kidney stones are a common urinary tract disorder that occurs primarily in middle aged men in developed countries. [1] When the stones are dislodged, passage through the ureter results in considerable pain. Kidney stones range from round structures a few millimeters in size to large staghorn shaped calculi which remain lodged in the kidney. There are many different types of stones that form in the human kidney: weddellite (calcium oxalate dihydrate); whewellite (calcium oxalate monohyrdrate); apatite; brushite and uric acid. [2]. Weddellite and whewellite stones tend to be the most common.

The fundamental mechanism for the formation of kidney stones is not fully understood. Certain people are stone formers and others are not. Supersaturation of calcium oxalate ions in the urine is a necessary precondition for stone formation.[3]. Nearly all urine is supersaturated with respect to these ions, so other explanations are needed. Two main mechanisms for the formation of kidney stones have been advanced: kidney stones are formed primarily due to crystal growth [4]; the stones are formed by aggregation of many small crystals that are held together by an organic matrix [5,6]. The primary objective of this paper was to use low voltage scanning electron microscopy (LVSEM) and atomic force microscopy (AFM) to gather microstructural evidence to determine which mechanism is the most likely to cause kidney stones.

EXPERIMENTAL METHOD

Two whewellite stones were used in this study. One of the stones was a fragment and the other a complete stone. Both stones were cut using the ultramicrotomy technique.[7] The complete stone was polished to the nucleus and then microtomed to assure as flat a surface as possible for good imaging on the AFM and scanning electron microscope (SEM). An optical microscope was utilized to provide a better understanding of the appearance of the two stones under a range of different magnification and for navigational purposed in the LVSEM.

The stones were placed in beam embedding capsules, size 00 for the fragmented stone and size 3 for the complete stone. L.R. White Acrylic Resin Hard Grade was poured into the molds to embed the stones. The encapsulated stones were placed in a curing oven at 100 C for approximately 4 hours. After the epoxy had cured, the molds were removed from the embedded samples with a razor blade.

The complete stone was then polished using 12 μm and 3 μm aluminum oxide polishing paper. The polishing was stopped at frequent intervals to examine the surfaces with an optical microscope to determine if the nucleus had been reached. This could be monitored by noting the shape of the concentric rings surrounding the nucleus. [8]

Hamilton graduated from Arizona State University (ASU) in May of 1995 with a B.Sc. degree in physics. This reserch was performed during the summer of 1994 when he worked as part of a NSF sponsored research program at ASU. He is currently working as a Device Quality Engineer for Motorola in Chandler, Arizona. In his spare time, he can be found spending time with his lovely wife and two daughters. In addition, he enjoys hiking, hunting and avoiding his next kidney stone.

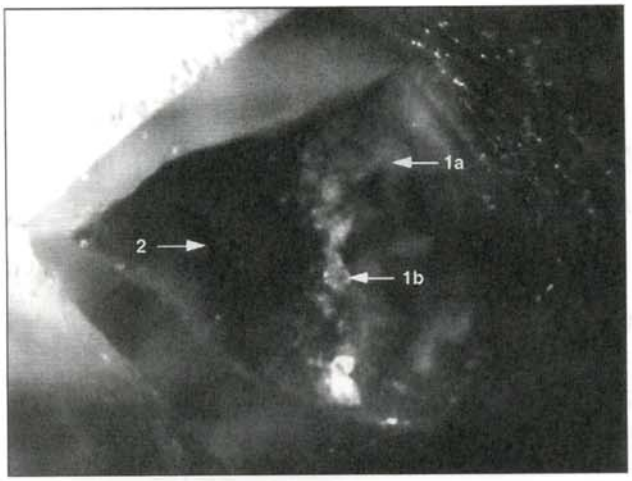

Figure 1
Optical image of the embedded fragmented stone studied in this work.

Once the nucleus was reached, the fragmented and polished complete stone were microtomed. To make the samples as flat as possible, the stones were first cut by a glass blade on the microtome machine until the surfaces of the stones were level. Then a diamond blade was used to remove several more microns to make the surface smoother. At the completion of this process, the excess epoxy from the molds was removed using a saw machine with a diamond saw blade. The excess epoxy was trimmed approximately 1.0 mm from the microtomed surface to allow the embedded samples to be mounted in the LVSEM and AFM. [9] Once the excess epoxy was removed, the samples were placed under an optical microscope to obtain an image for orientation of the microtomed surface in the LVSEM.

The stones were then taken to the University of Arizona Field Emission SEM facility to obtain multiple images at different magnifications. The magnification was limited by the residual charging. Low voltages were used to assure limited static charging of the specimens. The voltage that produced the best results was 2.5 kV. Using the capability of low magnification on the SEM and the optical images, navigation around the surface of the stone could be accomplished; many different parts of the surfaces could be viewed at different magnifications. This technique provided a good view of the morphology of the complete surface of the stones.

The stones were then taken to the Arizona State University AFM facility where images at several different resolutions were obtained. [10] The images were made using the contact mode. The AFM was capable of two different ranges of resolution: one head for 150 μm x 150 μm to 10 μm x 10 μm and another head for higher resolution. Both heads were used in this experiment. The higher resolution images were of more interest in determining the microstructure of the surface of the stones. The lower resolution images provided evidence that the structures seen at higher magnifications were part of the surface morphology.

Figure 1 shows an optical image of the fragmented pie shaped embedded stone. At the wider end and in the middle of the stone, marked by arrows 1a and 1b respectively, the structure appears as if it were formed by crystal growth. However, in the smaller section of the stone, marked by arrow 2, it is not apparent that crystal growth has occurred. The stone is not uniform in its morphology since the larger part of the stone and the smaller part differ.

The LVSEM image of the same stone is shown in Figure 2a. An apparent crystal growth at the top of the image is marked by arrow 1. The low magnification did not allow us to determine if the stone is a solid crystal. Behind the visible structure, marked by arrow 1, plates of stone are noticeable. The plated structures have been seen in previous experiments on kidney stones. They are indicative of aggregation. [6] The LVSEM image shown in Figure 2b provide stronger evidence that this specimen was

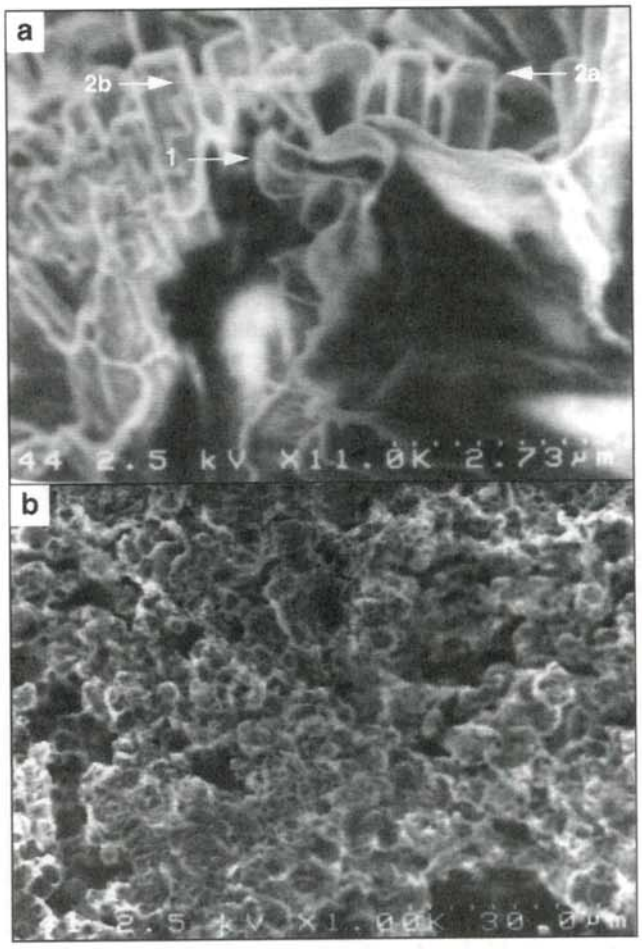

Figure 2
LVSEM image of the embedded fragmented stone at 2.5 kV a) magnification of 11 kX. b) magnification of 1 kX

formed by aggregation of many small crystals. The collection of many small crystals in this image indicate that crystal growth is not a likely explanation of the formation of the stone. The AFM images, seen in Figures 3a and 3b are consistent with these findings. Figure 3a shows common of aggregation. The arrows 1a and 1b mark places on the right side of the image where individual crystals are randomly gathered.

The lack of uniformity in the morphology of the complete image shown in Figure 3a is notable. It provides further evidence that this stone is made up of small crystals, held together by some adhesive agent. In Figure 3b, a higher

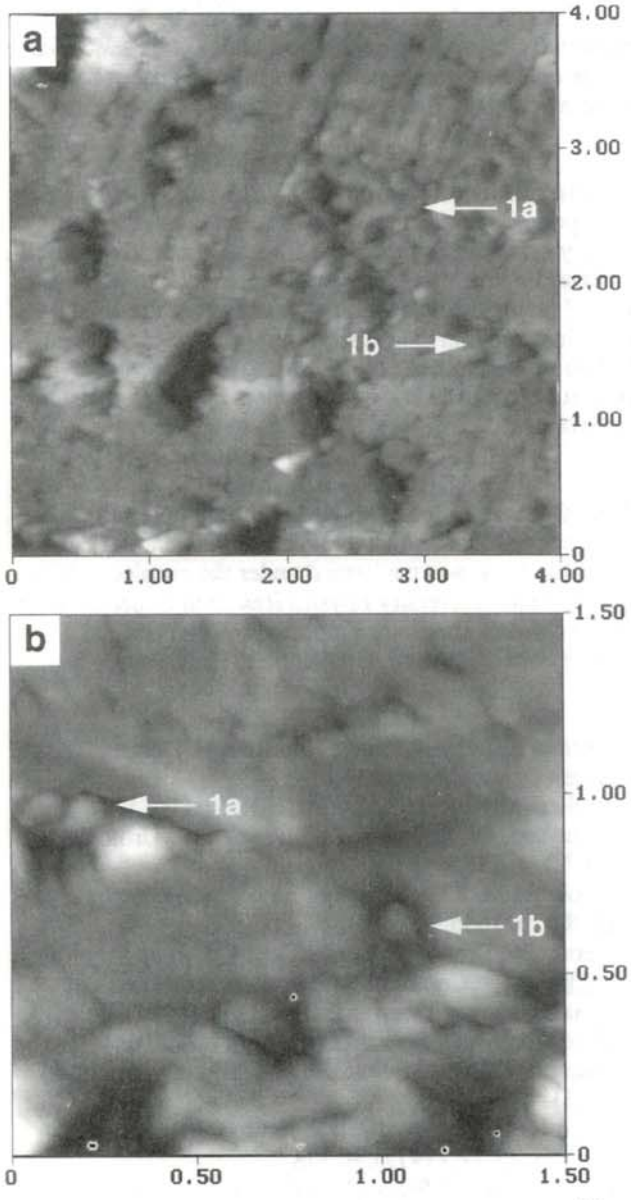

Figure 3
AFM image of the embedded fragmented stone. Arrows 1a and 1b show collections of single crystals. a) 4 µm resolution. b) 1 µm resolution.

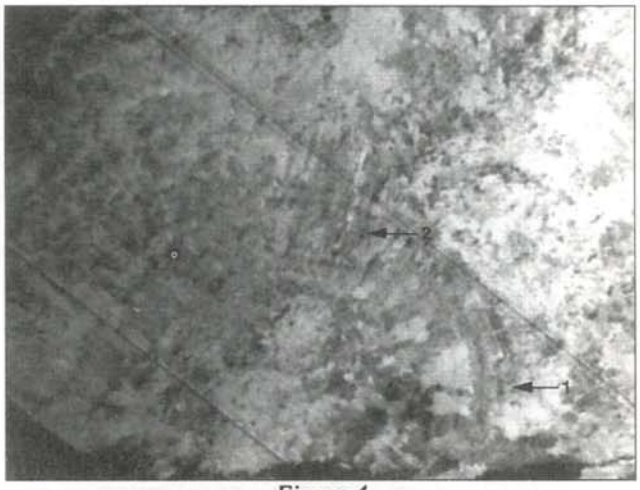

Figure 4
Optical image of the complete embedded stone studied in this work. Arrows 1 and 2 indicate concentric rings and radial striations repsectively.

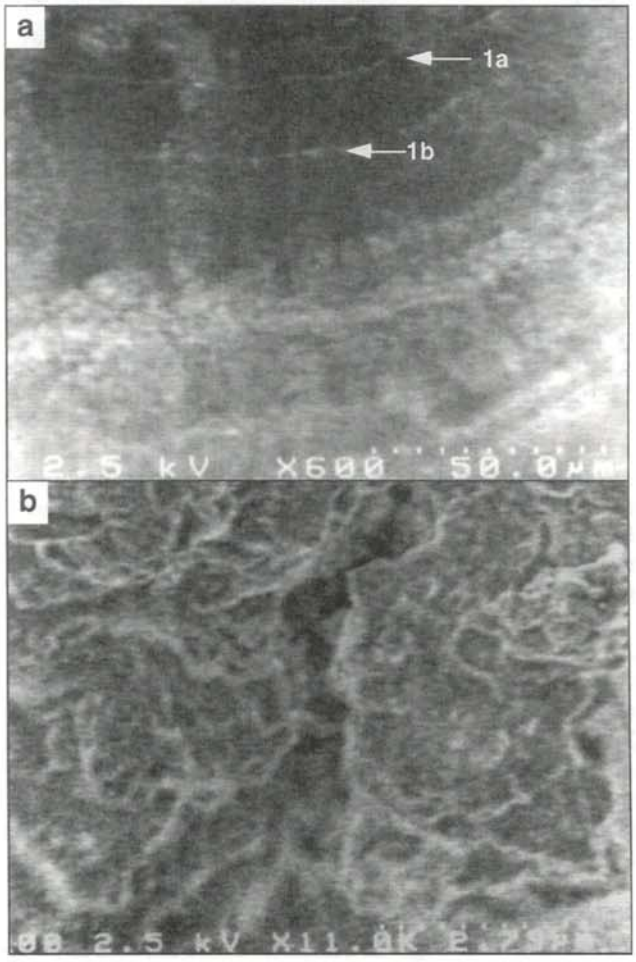

Figure 5
LVSEM image of the complete stone at 2.5 kV. a) 600 X magnification. Arrows 1a and 1b mark the concentric rings. b) 11 kX magnification.

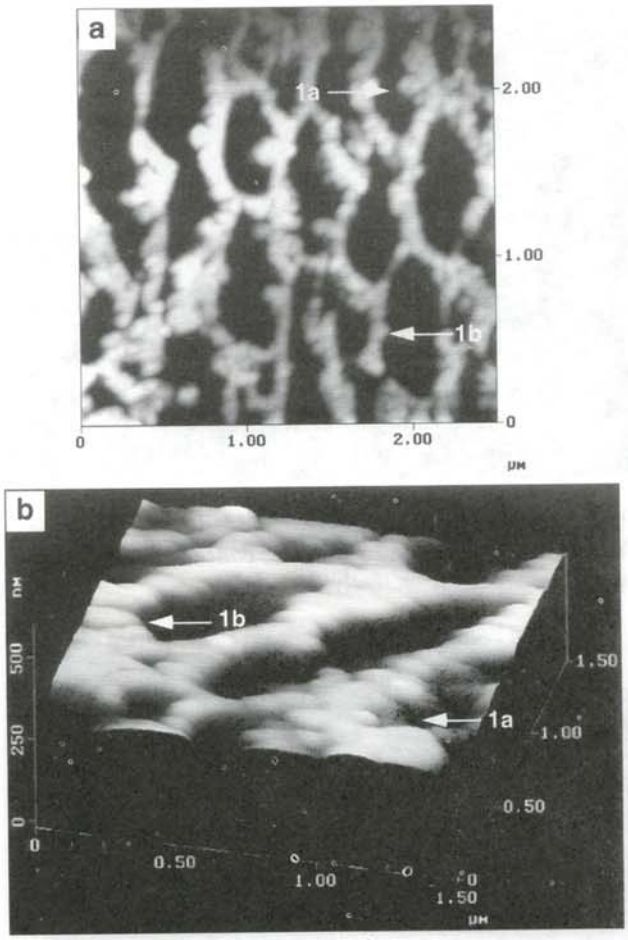

Figure 6
AFM image of the complete embedded stone a) 2 μm resolution. Arrows 1a and 1b show local crystal structure. b) surface image at 1.5 μm resolution.

resolution image, the randomness of the crystals becomes more apparent. Arrows 1a and 1b indicate regions where the sizes of these crystals are more noticeable. The average size of the crystals sown in Figure 3b is approximately 200 Å.

An optical image of the complete embedded stone is shown in Figure 4. This figure displays concentric rings, marked by arrow 1, and radial striations, marked by arrow 2, surrounding the nucleus. In Figure 5a, these concentric rings, marked by arrows 1a and 1b, are even more apparent due to the higher magnification. It has been argued that these concentric rings accompanied by radial striations represent successive stages of growth or aggregation. [6]

Figure 5b is an LVSEM image of the vicinity of the nucleus shown in Figures 4 and 5a. There appears to be no aggregation of crystals in this image, perhaps due to the low resolution of the image. The image does show porosity and some randomness in the morphology of the surface of the stone, possibly indicating that the stone is not a complete crystal. Crystal growth cannot be totally ruled out due to some of the uniformity of the mircostructure of the stone's surface. An AFM image close to the nucleus (Figure 6a) shows many small crystalline structures, marked by arrows 1a and 1b, which seem to be stuck together or stacked on top of one another. The way that the crystals seem to be stacked on top of one another signifies that the stone may be an aggregation of many small crystals. The spaces between the crystals in Figure 6a provide further evidence that the stone is not a complete crystal. These crystals in this image are also approximately 200 Å in size. Figure 6b, a surface image of the same area as Figure 6a, but at higher magnification and orientation, shows the stacks of crystals. The spaces between the crystals are again noticeable. It is conceivable that there is an organic matrix that fills the spaces between the small crystals.

SUMMARY

The observations obtained with LVSEM and AFM support the hypothesis that aggregation of small crystals is the primary mechanism behind the formation of kidney stones. The manner in which the crystals were stuck together and stacked on top of each other, as well as how the crystals were clustered together in seemingly random fashion in the two stones studied provide strong evidence that random aggregation is the mechanism by which the stones were formed.

ACKNOWLEDGMENTS

The author wishes to acknowledge the support and guidance of Don Eisenhower, Farhad Shaapur and Peter Rez. This work was performed under the auspices of the Arizona State University Physics Research Experience for Undergraduates Program, supported by the National Science Foundation and Arizona State University.

REFERENCES

* Current address of author: Hamilton H. Dorian, 2725 S. Karen Drive, Chandler, AZ 85248.

1. R. Sierakowski, B. Finlayson, R.R. Landes, C.D. Finlayson, N. Sierakowski, Investigative Urology, 15, (1978), p. 438.
2. Kookmin M. Kim, Scanning Electron Microscopy, 4, (1982), p. 1635.
3. George W. Drach, ed, Series Title: Common Problems in Urology, "Common Problems in Infections and Stones", Mosby Year Book, St. Louis, (1992), p. 2085.
4. Hidenobu Iwata, Shouzo Iio, Shunji Nishio and Masafumi Takeuchi, Scanning Microscopy, 6, (1992), p. 231.
5. Jorge J. Leal and Birdwell Finlayson, Investigative Urology, bf 14, (1977), p. 278.
6. L.U. Ogbuji and Birdwell Finlayson, Investigative Urology, 19, (1981), p. 182.

7. T.F. Malis and D. Steele, "Workshop on Specimen Preparation for TEM of Materials II", Ultramicrotomy for Materials Science, R. Anderson, ed., Materials Research Society, Pittsburgh, 199, (1990), p. 1
8. P. Rez, private communication.
9. F. Shaapur, P. Rez, D.R. Yaniv and G.W. Drach, (to be published).
10. P.K. Hansma, V.B. Elings, O. Marti, C.E. Bracker, Science, 242, (1988), p. 209.

FACULTY SPONSOR

Professor Peter Rez
Department of Physics and Astronomy
Arizona State University
Tempe, AZ 85287-1504
Rez@csss.la.asu.edu

PREDICTION OF THE VIBRATIONAL MODES OF SILICON CLATHRATE

Sumit K. Daftuar*
Department of Physics and Astronomy
Arizona State University
Tempe, AZ 85287-1504
received September 12, 1994

ABSTRACT

Quantum molecular dynamics techniques were used to predict the frequencies of the Γ point phonons of silicon (34) in the clathrate structure. These frequencies were compared to those predicted for the diamond phase of silicon. A wave number value for the highest frequency Γ point phonon of silicon (34) clathrate of approximately 493 cm^{-1}, shifted by 28 cm^{-1} from that of the diamond structure, is predicted.

INTRODUCTION

Silicon (34) Clathrate structure is a face-centered cubic system with 34 atoms in the primitive cell. The silicon atoms are arranged in dodecahedra and hexakaidecahedra in a 2:1 ratio. A detailed description can be found elsewhere [1].

Interest in the clathrate structures of silicon [2] has heightened as theoretical studies have demonstrated that they exhibit some unexpected properties. For example, it has been predicted that the energy of clathrates is very close to that of the lowest energy diamond structures of silicon, yet the clathrate structures have a significantly higher band gap. [1] These properties suggest that the clathrate structures of silicon may have important applications in electronic devices. The band gap predicted for silicon clathrates is approximately the same as that found in the porous structures of silicon, suggesting that porous silicon may be in some way related to a clathrate structure. This suggests that silicon clathrates may exhibit other interesting properties of porous silicon, such as photo luminescence.

The phonons of a crystal structure serve as a signature for the vibrational levels of the system. A knowledge of the vibrational frequencies of a crystal structure allows for the prediction of its Raman scattering spectrum. The Γ point phonons, those that correspond to the origin of reciprocal lattice space, were chosen for this study because these phonons have the same wave vector as the light photons, thus are the ones that would be detected by Raman spectroscopy.

METHOD

Quantum molecular dynamics techniques (QMD) [3] use the electronic structure of the material to calculate the energies of and the forces acting in crystal structures. These are needed to determine the phonon spectrum for the crystal. This "tight-binding-like model" [3] uses pseudo-atomic orbitals to determine the electronic Hamiltonian matrix elements. The Hellmann-Feynman theorem [3] is used to calculate the forces acting on the atoms in the crystal.

The equilibrium atomic positions within a crystal can be computed using dynamical quenching. This technique begins with an approximate equilibrium structure, in which the atoms are at rest. The atoms are then allowed to move in response to the forces within the crystal. The system gains kinetic energy as the atoms move. This energy is removed whenever a maximum value of the kinetic energy is reached. Eventually, the atoms reach a minimum potential energy configuration, where the net

Sumit is a senior physics and mathematics concentrator at Harvard University, where he is also co-president of the Society of Physics Students. This research was conducted in the summer of his sophomore year when he worked as part of an NSF sponsored research program at Arizona State University. In his spare time, he tries to keep up with politics and current events, and he also plays basketball and bridge. He is planning to attend graduate school in mathematics next year and is currently applying to a number of graduate programs. Sumit is a resident of Mesa, Arizona

force is on the atoms is zero.

Once the crystal's equilibrium structure has been determined, the phonon spectrum is determined by a method known as harmonic analysis. [4] The displacement of the atoms from the equilibrium configuration is given by:

$$X = (x_1^1, x_1^2, x_1^3, x_2^1, x_2^2, x_2^3, ..., x_N^1, x_N^2, x_N^3), \quad (1)$$

where the subscript denotes the atom number and the subscript gives the direction (x,y,z or 1,2,3). The potential energy of the system, V, can be expanded in a Taylor series about the equilibrium point:

$$V = V_o + \sum_n \sum_i \frac{\partial V}{\partial x_n^i} dx_n^i + \frac{1}{2!} \sum_n \sum_{i,j} \frac{\partial^2 V}{\partial x_n^i \partial x_p^j} dx_n^i dx_p^j + \dots . \quad (2)$$

Since the value of the potential energy can be shifted by a constant without changing the physical meaning, V_o can arbitrarily be set equal to zero. Since the system is at a minimum of the potential energy, the first-order shift in the energy caused by the displacement of any atom in any direction must be zero. This means that the second term in Equation 2 must be zero. Ignoring terms higher than second order, the Equation 2 becomes:

$$V = \frac{1}{2} \sum_n \sum_{i,j} \frac{\partial^2 V}{\partial x_n^i \partial x_p^j} dx_n^i dx_p^j \quad . \quad (3)$$

Thus, the force on the p^{th} atom in the j^{th} direction is given by:

$$F_p^j = -\frac{\partial V}{\partial x_p^j} = -\sum_n \sum_i \frac{\partial^2 V}{\partial x_n^i \partial x_p^j} dx_n^i . \quad (4)$$

Newton's second law becomes:

$$-\sum_n \sum_i \frac{\partial^2 V}{\partial x_n^i \partial x_p^j} dx_n^i = m_p \ddot{x}_p^j \ , \quad (5)$$

where m_p is the mass of the p^{th} atom.

If the system contains N atoms, then Equation 5 corresponds to 3N equations, which can be written in matrix notation as:

$$-\Phi X = M \ddot{X} \ , \quad (6)$$

where

$$X = \begin{bmatrix} x_1^1 \\ x_1^2 \\ x_1^3 \\ \cdots \\ x_N^1 \\ x_N^2 \\ x_N^3 \end{bmatrix}, M = \begin{bmatrix} m_1 & 0 & 0 & \cdots & 0 & 0 & 0 \\ 0 & m_1 & 0 & \cdots & 0 & 0 & 0 \\ 0 & 0 & m_1 & \cdots & 0 & 0 & 0 \\ \cdots & \cdots & \cdots & \cdots & \cdots & \cdots & \cdots \\ 0 & 0 & 0 & \cdots & m_N & 0 & 0 \\ 0 & 0 & 0 & \cdots & 0 & m_N & 0 \\ 0 & 0 & 0 & \cdots & 0 & 0 & m_N \end{bmatrix} \quad (7a)$$

$$\Phi = \begin{bmatrix} \frac{\partial^2 V}{\partial x_1^1 \partial x_1^1} & \frac{\partial^2 V}{\partial x_1^1 \partial x_1^2} & \frac{\partial^2 V}{\partial x_1^1 \partial x_1^3} & \cdots & \frac{\partial^2 V}{\partial x_1^1 \partial x_N^1} & \frac{\partial^2 V}{\partial x_1^1 \partial x_N^2} & \frac{\partial^2 V}{\partial x_1^1 \partial x_N^3} \\ \frac{\partial^2 V}{\partial x_1^2 \partial x_1^1} & \frac{\partial^2 V}{\partial x_1^2 \partial x_1^2} & \frac{\partial^2 V}{\partial x_1^2 \partial x_1^3} & \cdots & \frac{\partial^2 V}{\partial x_1^2 \partial x_N^1} & \frac{\partial^2 V}{\partial x_1^2 \partial x_N^2} & \frac{\partial^2 V}{\partial x_1^2 \partial x_N^3} \\ \frac{\partial^2 V}{\partial x_1^3 \partial x_1^1} & \frac{\partial^2 V}{\partial x_1^3 \partial x_1^2} & \frac{\partial^2 V}{\partial x_1^3 \partial x_1^3} & \cdots & \frac{\partial^2 V}{\partial x_1^3 \partial x_N^1} & \frac{\partial^2 V}{\partial x_1^3 \partial x_N^2} & \frac{\partial^2 V}{\partial x_1^3 \partial x_N^3} \\ \cdots & \cdots & \cdots & \cdots & \cdots & \cdots & \cdots \\ \frac{\partial^2 V}{\partial x_N^1 \partial x_1^1} & \frac{\partial^2 V}{\partial x_N^1 \partial x_1^2} & \frac{\partial^2 V}{\partial x_N^1 \partial x_1^3} & \cdots & \frac{\partial^2 V}{\partial x_N^1 \partial x_N^1} & \frac{\partial^2 V}{\partial x_N^1 \partial x_N^2} & \frac{\partial^2 V}{\partial x_N^1 \partial x_N^3} \\ \frac{\partial^2 V}{\partial x_N^2 \partial x_1^1} & \frac{\partial^2 V}{\partial x_N^2 \partial x_1^2} & \frac{\partial^2 V}{\partial x_N^2 \partial x_1^3} & \cdots & \frac{\partial^2 V}{\partial x_N^2 \partial x_N^1} & \frac{\partial^2 V}{\partial x_N^2 \partial x_N^2} & \frac{\partial^2 V}{\partial x_N^2 \partial x_N^3} \\ \frac{\partial^2 V}{\partial x_N^3 \partial x_1^1} & \frac{\partial^2 V}{\partial x_N^3 \partial x_1^2} & \frac{\partial^2 V}{\partial x_N^3 \partial x_1^3} & \cdots & \frac{\partial^2 V}{\partial x_N^3 \partial x_N^1} & \frac{\partial^2 V}{\partial x_N^3 \partial x_N^2} & \frac{\partial^2 V}{\partial x_N^3 \partial x_N^3} \end{bmatrix} \quad (7b)$$

Equation 6 can be rewritten as:

$$-M^{-1} \Phi X = \ddot{X} \ , \quad (8)$$

where $M^{-1}\Phi$ is symmetric. Equation 8 is linear and has normal mode solutions of the form:

$$X(t) = X(0)\, e^{i\omega t} \ . \quad (9)$$

Using the normal mode solutions in Equation 8 gives:

$$M^{-1} \Phi X = \omega^2 X \ . \quad (10)$$

The squares of the normal mode vibrational frequencies of the phonons are found by diagonalizing the $M^{-1}\Phi$ matrix. To do this, we first had to determine the matrix elements of Φ. Each atom was displaced slightly from equilibrium (while the other atoms were in their equilibrium positions) and the force on each atom due to all the others was computed. The corresponding matrix element was found by dividing each force by the displacement. Because any finite displacement would result in small anharmonic contributions to the forces, two Φ matrices were computed: one derived from positive displacements of the atoms; one derived from negative displacements of the atoms. These two matrices were then averaged (thereby cancelling the third-order contributions to the potential energy). The resulting Φ matrix was multiplied by the inverse mass matrix M^{-1}, and diagonalized to obtain the frequencies.

RESULTS AND DISCUSSION

The QMD techniques of Sankey and Niklewski were used to predict the phonon frequencies of bulk silicon and the silicon clathrate structure. A comparison of the frequencies obtained for these two structures allowed us to determine the shift in phonon frequency for silicon clathrate relative to the diamond structure of bulk silicon.

To determine the elements of the Φ matrix, an electronic structure calculation was done that involved an evaluation of the integrals of electron energies over the Brillouin zone. These integrals were evaluated approximately using the k-point method. [5] In this method, the value of the

energy at a few judicioulsy chosen "k-points', or reciprocal lattice vectors, is used to approximate the average value of the energy over the entrie Brillouin zone. As the number of k-points increases, the approximation converges to the exact value of the integral. Because of the computational demands of finding the electron energies for the clathrate structure, we had to determine how many k-points were needed for convergence to occur. For the diamond structure of silicon, the three optic Γ point phonons are theoretically perfectly degenerate. We found that the average value of the predicted phonon frequency for the three optic Γ point phonons never differed by more than 0.2 cm^{-1} from their mean values and converged to within 0.1 cm^{-1} when 216 k-points were used. Phonon 'frequencies' are commonly given in units of inverse centimeters; to convert them into actual frequencies, multiply by the speed of light. The results are shown in Table 1. The unit cell for the clathrate structure is much larger than that of the diamond structure, so the Brillouin zone of the clathrate structure is much smaller. We felt that using only 8 k-points would be sufficient for the clathrate structure, giving a k-point density that is of same order, but somewhat smaller than the k-point density required for convergence in bulk silicon.

For the diamond structure, we found that the equilibrium configuration was one in which the primitive *fcc* cell had atoms spaced 2.382 Å apart. This structure was found to have three Γ point optical phonons, two transverse and one longitudinal, with $\omega = 541$ cm^{-1}. The experimentally measured value is 521 cm^{-1}. The other three eigenvalues were zero and corresponded to translations of the crystal in each of the three spatial directions.

For the clathrate structure, there were 102, (34 x 3), vibrational frequencies, including three values for $\omega = 0$ corresponding to translations of the crystal. The vibrational density of states is displayed in Figure 1. The delta functions of frequency are smoothed out using a Gaussian function with width 5 cm^{-1}. The highest frequency phonons in this structure have a frequency of 513 cm^{-1}, a downward shift of 28 cm^{-1} from the diamond structure of silicon. Because the model used is well suited for predicting shifts in frequencies, we predict an actual frequency of

Number of k-points	Predicted Phonon Frequency cm^{-1}
1	787.12
4	541.07
64	540.39
216	540.64
512	540.69
1372	540.66
4096	540.70

Table 1

Predicted average Γ point optic phonon frequency of bulk silicon vs. number of k-points used to approximate the integral in the Brillouin zone.

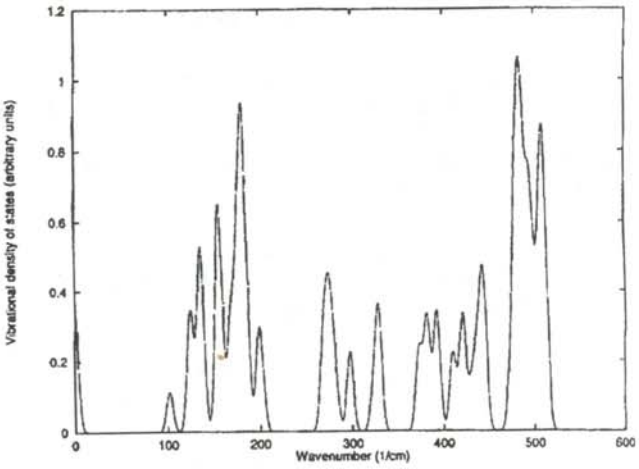

Figure 1

Theoretical density of states for silicon(34)clathrate. The highest frequency peak occurs at 513 cm^{-1}.

(521cm^{-1} - 28cm^{-1}) = 493 cm^{-1} for the highest frequency phonons of the clathrate structure. (We are primarily interested in the highest frequency normal mode because this mode, in which the atoms move back and forth directly towards and away from one another, corresponds to a similar mode in the diamond structure).

This highest frequency peak in the Raman spectrum of porous silicon is 514 cm^{-1}, only a 7 cm^{-1} downward shift from diamond structure silicon. [6] These results are quite different from the 28 cm^{-1} we found in the shift for calthrate structure. There does not appear to be a close connection between the clathrate structure of silicon and porous silicon, even though the electronic band gaps of these two materials are nearly identical.

A previous calculation of the vibrational of this structure used the Keating model. [7,8] In this model, the potential energy is expressed in terms of two force constants, α and β, that are derived from experimental results. The parameter α represents the bond stretching force constant while β represents the bonding bending force constant. This calculation yielded highest frequency phonons with $\omega = 517$ cm^{-1}, significantly different from our value of 493 cm^{-1}. The Keating model calculation, which used a β to α ratio of 0.2, making the stretching force constant dominant. The authors may have underestimated the importance of the bond-bending forces because the bond angles in clathrate often have significant deviations from the ideal value of 109.5° found in the diamond structure. In the clathrate structure, the bond angles vary from 104° to 120°; 18% of the bonds between 109° and 110° and 62% are between 107° and 112°. The authors have acknowledged that their choice for the ratio of the force constants is somewhat arbitrary. A more consistent procedure for determining the Keating force constants resulted in a ratio of 0.285, but this ratio may still not be appropriate for studying clathrate structures because it is based on the diamond structure. [9]

ACKNOWLEDGMENTS

The author expresses thanks to Alex A. Demkov, Otto F. Sankey and James P. Lewis for their assistance and guidance. This work was preformed under the auspices of the Arizona State University Physics Research Experience for Undergraduates Program, supported by the National Science Foundation and Arizona State University.

REFERENCES

* Present Address of the author: Department of Physics, Harvard University, Cambridge, MA 02138.
1. G. B Adams, M. O'Keefe, A.A. Demkov, O.F. Sankey and Y. Juang, Phys. Rev. B, 48, (1994), p. 8048.
2. J.S. Kaspar, P. Hagenmuller, M. Pouchard and C. Cros, Science, 150, (1965), p. 1713.
3. O.F. Sankey and D.J. Niklewski, Phys. Rev., B 40, (1989), p. 3979.
4. M. Born and K. Huang, *Dynamical Theory of Crystal Lattices*, Oxford University press, (1954).
5. H.J. Monkhurst and J.D. Pack, Phys. Rev. B 12, (1978), p. 5188.
6. M.S. Brandt, M.D. Fuchs, M. Stutzmann, J. Weber and M. Cardona, Solid State Commun., 81, (1992), p. 307.
7. R. Alben, D. Weaire, J.E. Smith, Jr. and M.H. Brodsky, Phys. Rev. B 11, (1975), p. 2271.
8. P.N. Keating, Phys. Rev., 145, (1966), p. 637.
9. R.M. Martin, Phys. Rev. B 1 , (1970), p. 4005.

FACULTY SPONSOR

Dr. Otto Sankey
Department of Physics and Astronomy
Arizona State University
Tempe, AZ 85287-1504
otto.sankey@asu.edu